Electronic Supplementary Information

Stepwise MXene and MOF Conversion Assisted Ultrathin Dual-Carbon Protected V_2O_3 Nanosheets for Ultrafast and Durable Zn-Ion Storage

Xiaolin Ma[a,1], Ke Han[a,1], Hongxing Li [a,1], Lulu Song[a], Yuan Lin[a], Liangxu Lin[a], Yang Liu[a], Yi Zhao[a,], Zhen Yang [a,*], Wei Huang[b,*]*

[a]Strait Institute of Flexible Electronics (SIFE, Future Technologies), Fujian Key Laboratory of Flexible Electronics, Fujian Normal University and Strait Laboratory of Flexible Electronics (SLoFE), Fuzhou 350117, China

[b]Frontiers Science Center for Flexible Electronics (FSCFE), MIIT Key Laboratory of Flexible Electronics (KLoFE), Northwestern Polytechnical University, Xi'an 710072, China

[1]These authors contributed equally to this work.

*Corresponding Author

E-mail: ifeyzhao@fjnu.edu.cn; ifezhyang@fjnu.edu.cn; vc@nwpu.edu.cn

Experimental Section

Synthesis of C@V_2O_3@C nanosheets

First, V_2CT_x MXene was prepared by etching V_2AlC precursor with HF acid followed with delamination process and freeze-drying.[1] For MXene conversion, V_2CT_x was annealled at 600 ^oC for 3 h under CO_2 atomosphere to achieve C@V_2O_3 composite. Next, MXene-derived C@V_2O_3 product was mixed with terephthalic acid (H_2BDC) ligand (weight ratio of 1:1), sealed in a quartz tube under vacuum, and calcinated at 380 ^oC for 6 h. Finally, as-prepared C@V_2O_3@MOF was carbonized at 700 ^oC for 3 h under Ar atmosphere to synthesize C@V_2O_3@C composite. To tailor the thickness of MOF-derived outer carbon, C@V_2O_3@C-2h and C@V_2O_3@C-24h samples were prepared under the same procedure except the different weight ratios of C@V_2O_3 and H_2BDC and conversion times of 1:1 for 2 h and 1:3 for 24 h, respectively. In this manuscript, the C@V_2O_3@MOF and C@V_2O_3@C composites were related to the samples through 6 h MOF conversion time. Pure V_2O_3 was obtained by direct oxidization of V_2CT_x MXene at 400 ^oC for 3 h in air atomosphere followed with Ar/H_2 reduction at 500 ^oC for 3 h. MXene-derived carbon was synthesized by etching C@V_2O_3 with concentrated nitric acid for 24 h.

Materials Characterization

The morphology and structure properties of these composites were investigated through transmission electron microscopy (TEM, FEI Tecnai F20), scanning electron microscopy (SEM, SU-8010), and X-ray diffraction (XRD, Shimadzu Miniflex600). The thickness of samples were analysized through atomic force microscopy (AFM, Bruker Dimension Edge). The surface area and porosity property of samples were performed through a Brunauer-Emmett-Teller surface area analyzer (Quantachrome Autoscorb-iQ2-XR). The weight contnet of V_2O_3

in these composites were determined via thermogravimetry analyses (NETZSCH STA449C) from 30 to 800 ℃ in Air. The surface chemical composition was identified by X-ray photoelectron spectroscopy (XPS, ESCALAB 250 Xi).

DFT Calculation

The Vienna Ab Initio Package (VASP) was employed to perform all the density functional theory (DFT) calculations within the generalized gradient approximation (GGA) using the Perdew, Burke, and Enzerhof (PBE) formulation.[2-4] The projected augmented wave (PAW) potentials were applied to describe the ionic cores and take valence electrons into account using a plane wave basis set with a kinetic energy cutoff of 450 eV.[5, 6] Partial occupancies of the Kohn–Sham orbitals were allowed using the Gaussian smearing method and a width of 0.05 eV. The electronic energy was considered self-consistent when the energy change was smaller than 10^{-5} eV. A geometry optimization was considered convergent when the force change was smaller than 0.03 eV/Å. Grimme's DFT-D3 methodology was used to describe the dispersion interactions.[7] The vacuum spacing perpendicular to the plane of the structure is 20 Å. The Brillouin zone integral utilized the surfaces structures of 2×2×1 monkhorst pack K-point sampling. The Charge density difference of system:$\Delta\rho = \rho_{total} - \rho_A - \rho_B$, where ρ_{total} is the charge density of Binding systems, ρ_A and ρ_B is the sub charge density. Finally, the adsorption energies (Eads) were calculated as Eads= Ead/sub -Ead -Esub, where Ead/sub, Ead, and Esub are the total energies of the optimized adsorbate/substrate system, the adsorbate in the structure, and the clean substrate, respectively. Ions pathway can be calculated using the nudged elastic band (NEB) method with the transition state of an elementary reaction step. In the NEB method, the path between the reactant (s) and product (s) was discretized into a series structural images. The intermediate images were relaxed until the perpendicular forces were smaller than 0.05 eV/Å.

Electrochemical Measurements

The zinc-ion storage performance of these composites was studied in 2032 coin-type cells, which were assembled in an air atmosphere. The working cathode was fabricated by mixing C@V_2O_3@C powder (70 wt%), carbon black (20 wt%), and polyvinylidene fluoride (10 wt%) in N-methyl pyrrolidone. Then, the obtained mixture slurry was evenly coated on a carbon cloth and dried at 80 ℃ for 24 h. V_2CT_x, V_2O_3, C@V_2O_3 electrodes were prepared through the same procedure. The loading mass of each cathode was 1.2-1.6 mg/cm^2 with a tapping density around 1.08 g/cm^3. Besides, high loading mass of 3 and 5 mg/cm^2 were also prepared to realize high areal capacity. Zn foil (various mass from 11.2 to 25.6 mg/cm^2), $Zn(CF_3SO_3)_2$ aqueous solution (3 M) and glass fiber membrane (Whatman GF/D, USA) were used as the anode, electrolyte, and separator, respectively. The negative/positive (N/P) ratio for battery test was in the range from 30: 1 to 7: 1 in this work. A CHI660C electrochemical workstation was used for cyclic voltammetry test (scan rates from 0.2 to 5 mV s^{-1}) and electrochemical impedance spectroscopy (frequency range of 100 kHz to 0.01 Hz.). The cycling performance, rate capability, and galvanostatic intermittent titration technique test of these electrode was conducted in the NEWARE battery testing system in the voltage range of 0.2-1.8 V. All the above tests were measured at room temperature. *In-situ* XRD test was performed through a 2023 coin-type cell with an open window.

For the assembly of quasi solid-state ZIBs, the hydrogel membrane was first obtained by mixing 3 g acrylamide, 30 mg potassium persulfate and 4 mg N,N'-Methylenebisacrylamide with 20 mL deionized water, drying at 60 ^{o}C for 2-3 h at a costom-designed mold, and immersing in the $Zn(CF_3SO_3)_2$ (3 M) solution. The pounch cells was constructed with zinc foil as anode, C@V_2O_3@C as cathode, and hydrogel membrane as the seperator and electrolyte, which were packaged with polyimide films.

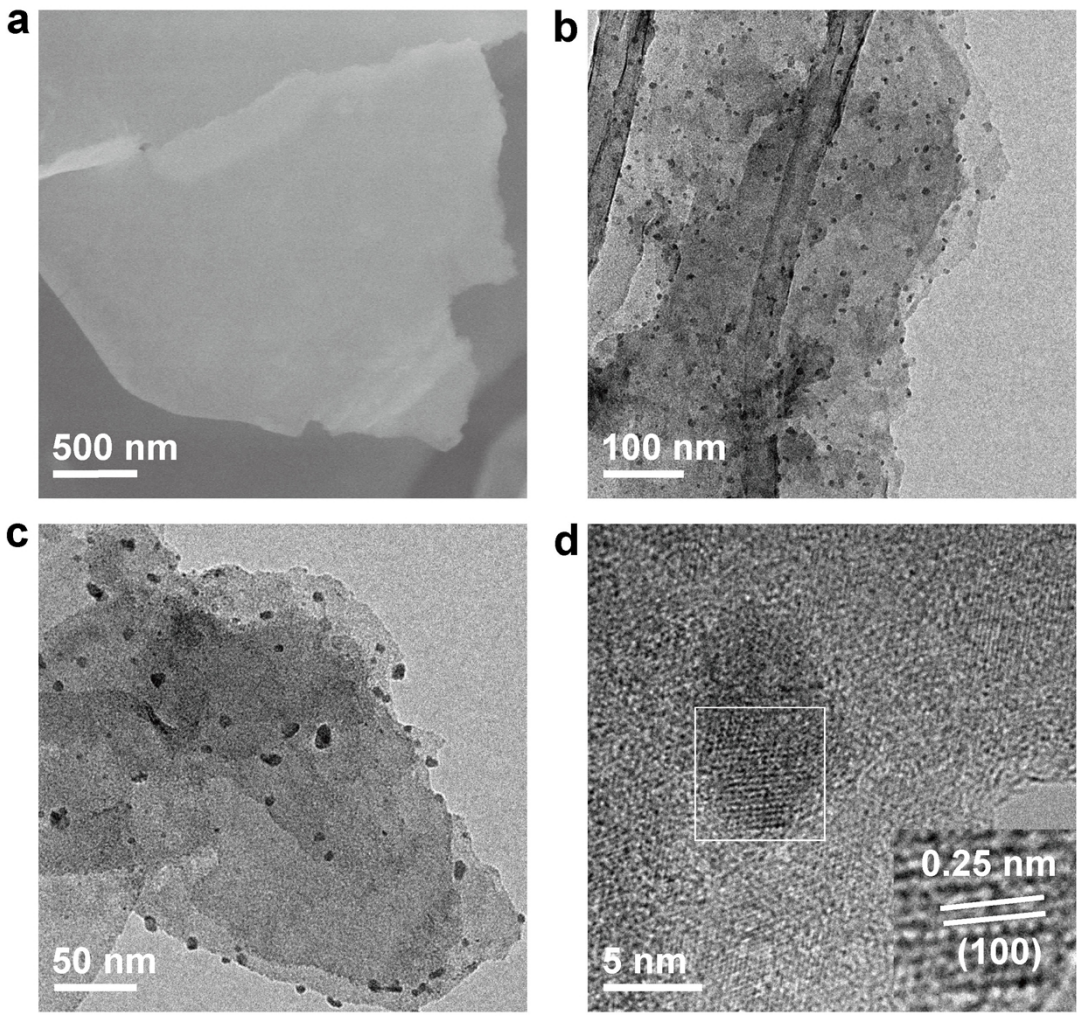

Fig. S1 (a) SEM and (b-d) TEM images of V_2CT_x MXene.

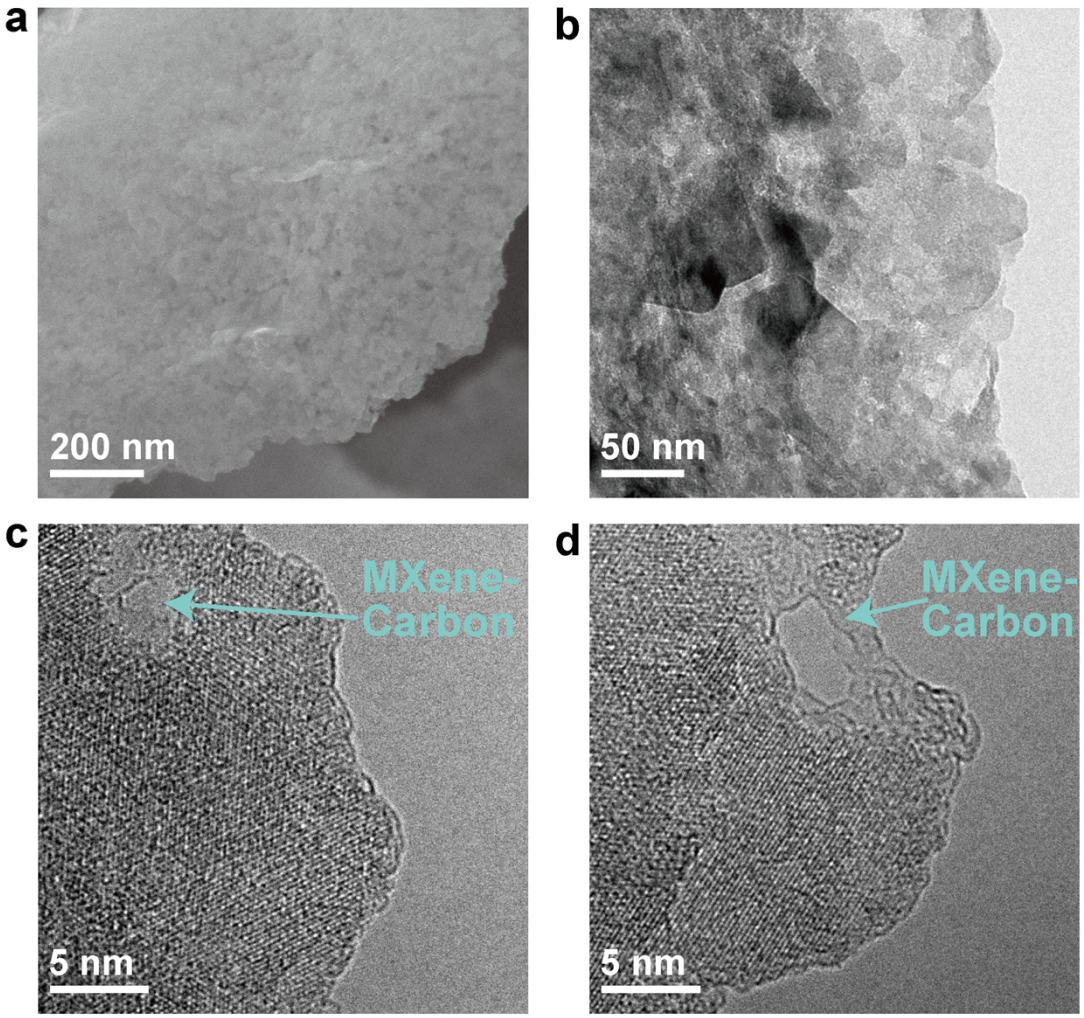

Fig. S2 (a) SEM and (b-d) TEM images of MXene-derived C@V_2O_3 composite.

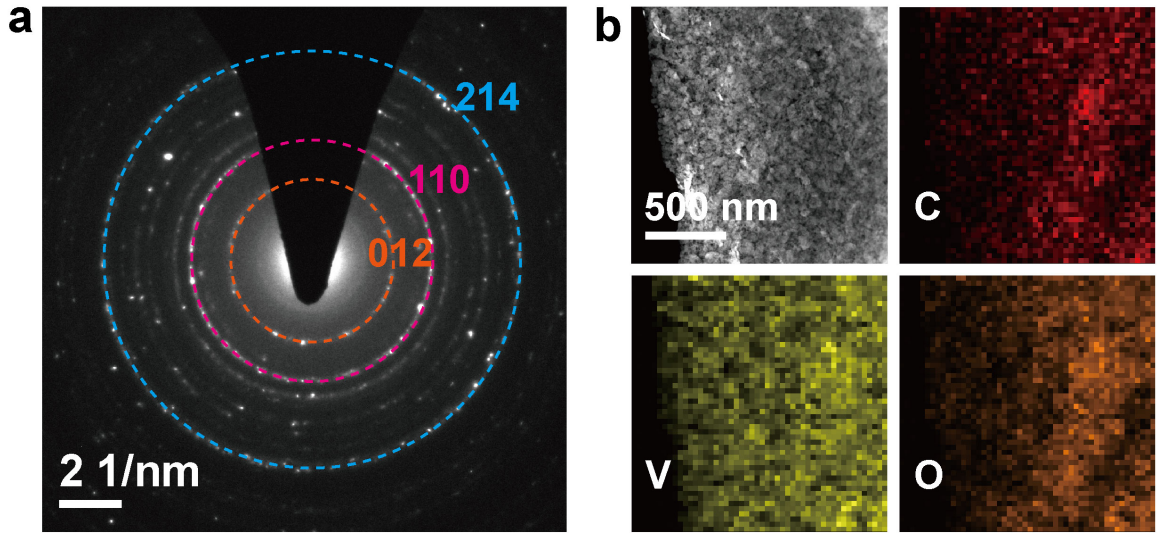

Fig. S3 (a) Selected area electron diffraction (SAED) pattern and (b) element mappings of C, V, and O for C@V_2O_3 composite.

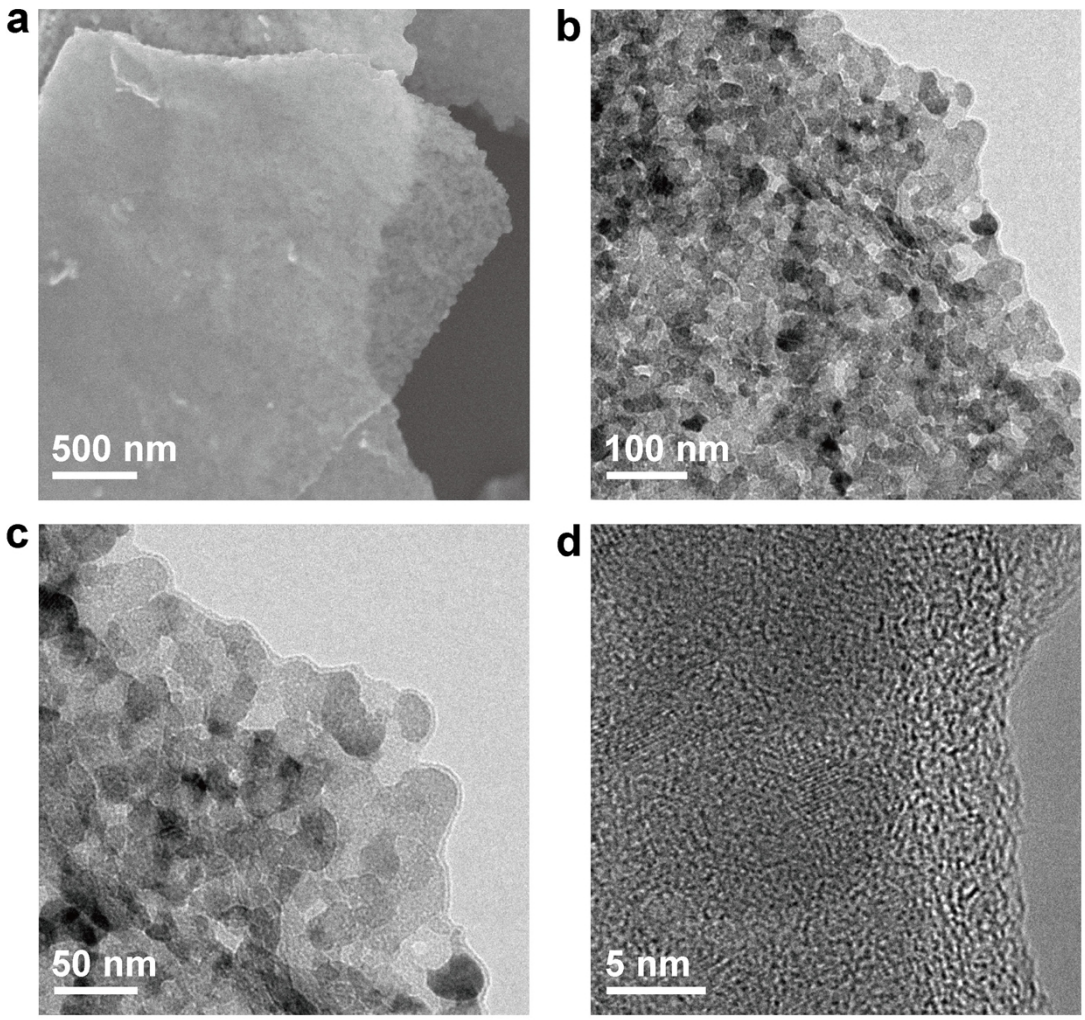

Fig. S4 (a) SEM and (b-d) TEM images of C@V_2O_3@MOF composite.

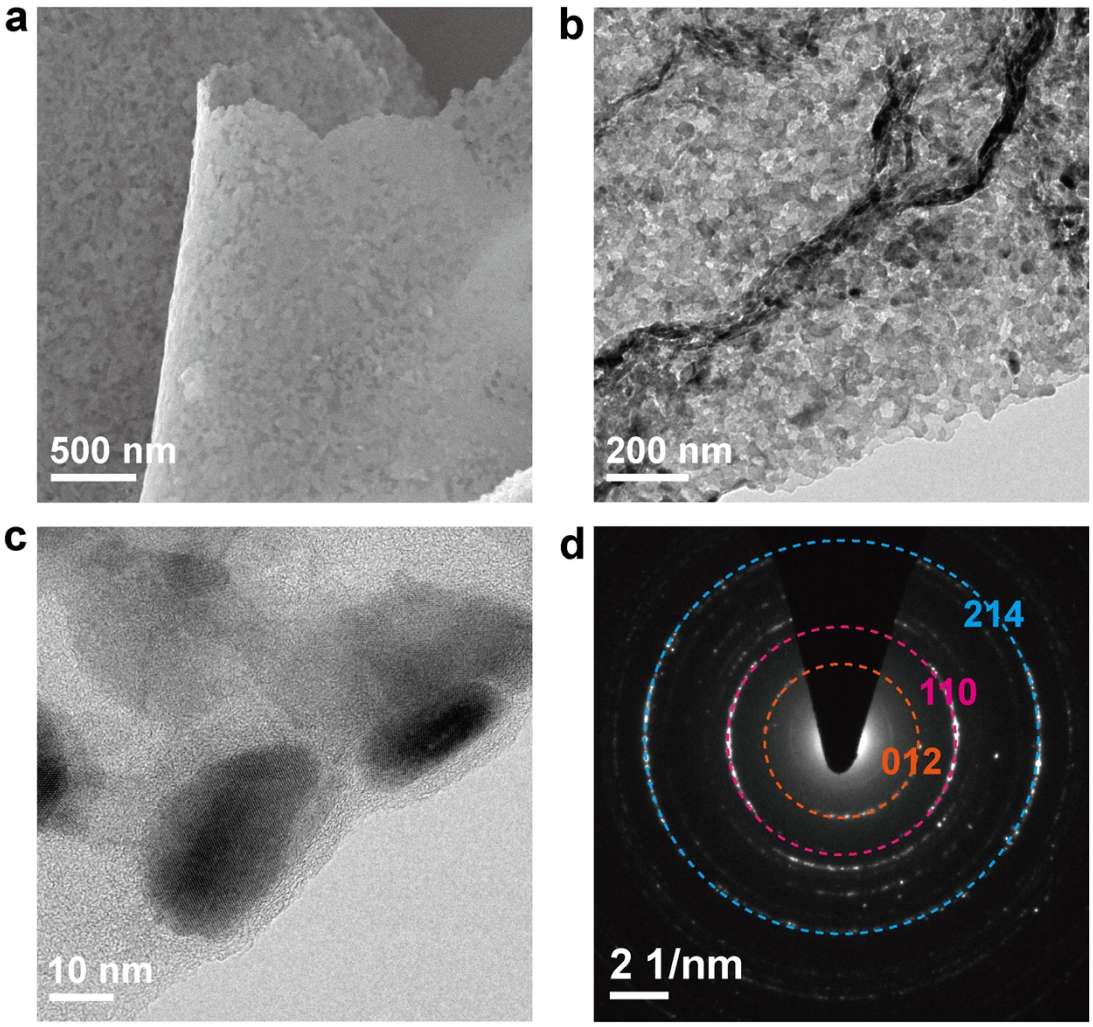

Fig. S5 (a) SEM, (b-c) TEM images, and (d) SAED pattern of C@V_2O_3@C composite.

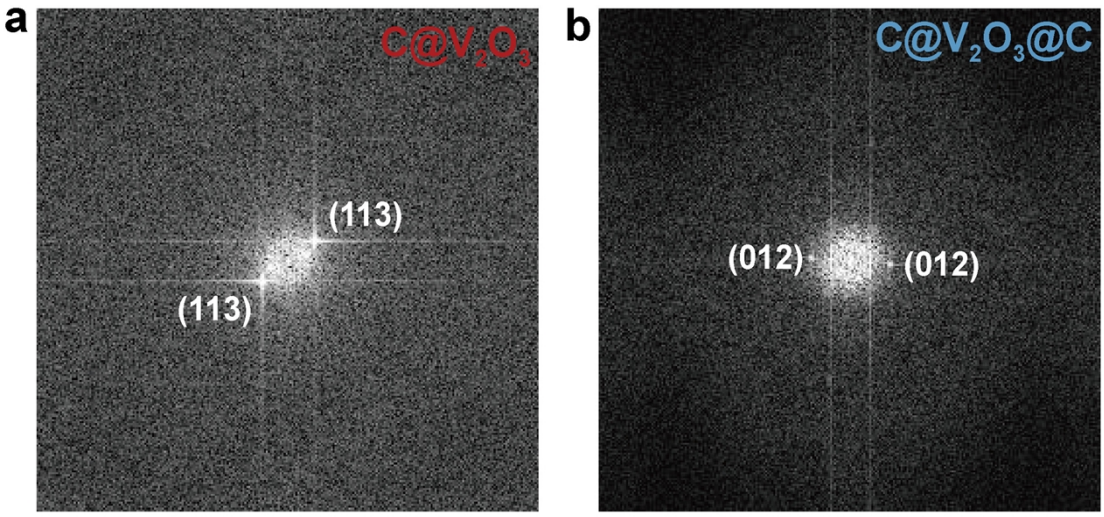

Fig S6 FFT images of (a) $C@V_2O_3$ and (b) $C@V_2O_3@C$ composites.

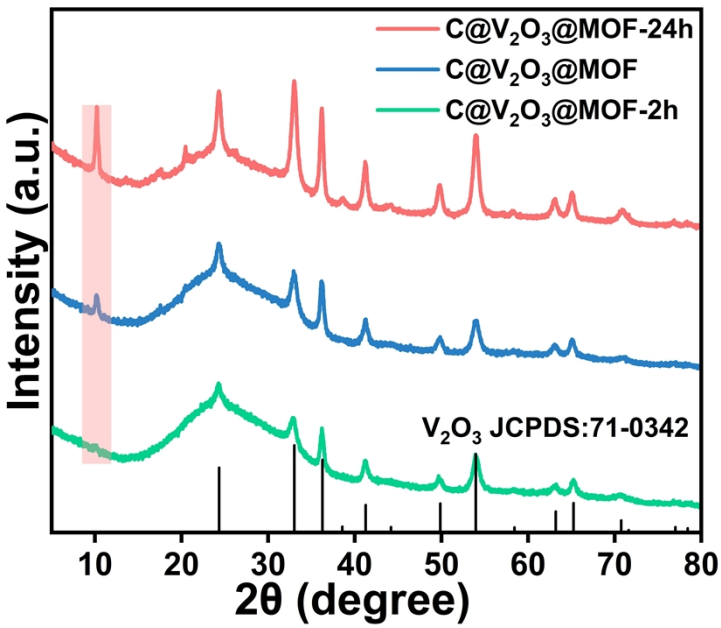

Fig. S7 XRD profiles of C@V_2O_3@MOF-2h, C@V_2O_3@MOF and C@V_2O_3@MOF-24h composites under various MOF conversion times. The C@V_2O_3@MOF represents 6 h conversion time.

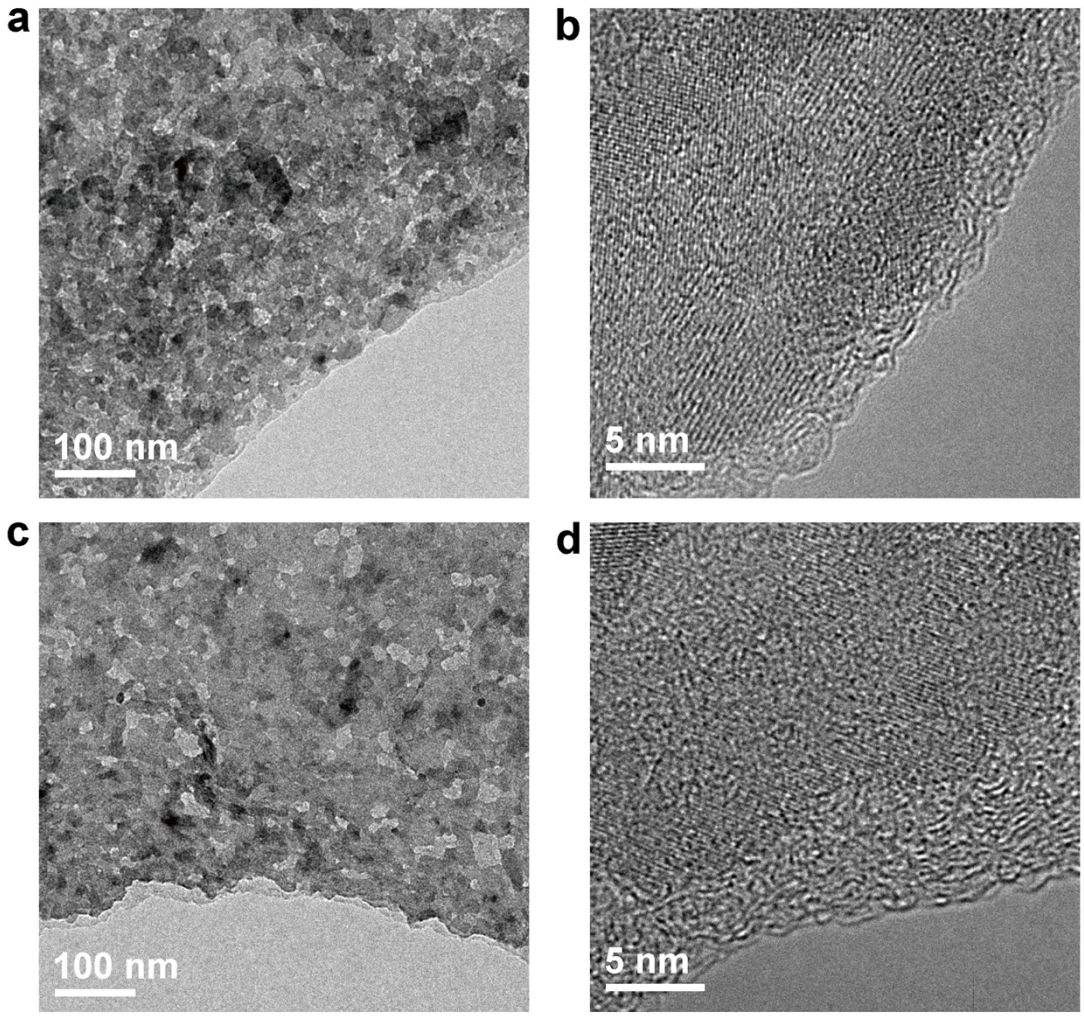

Fig. S8 TEM images of (a-b) C@V_2O_3@C-2h and (c-d) C@V_2O_3@C-24h composites.

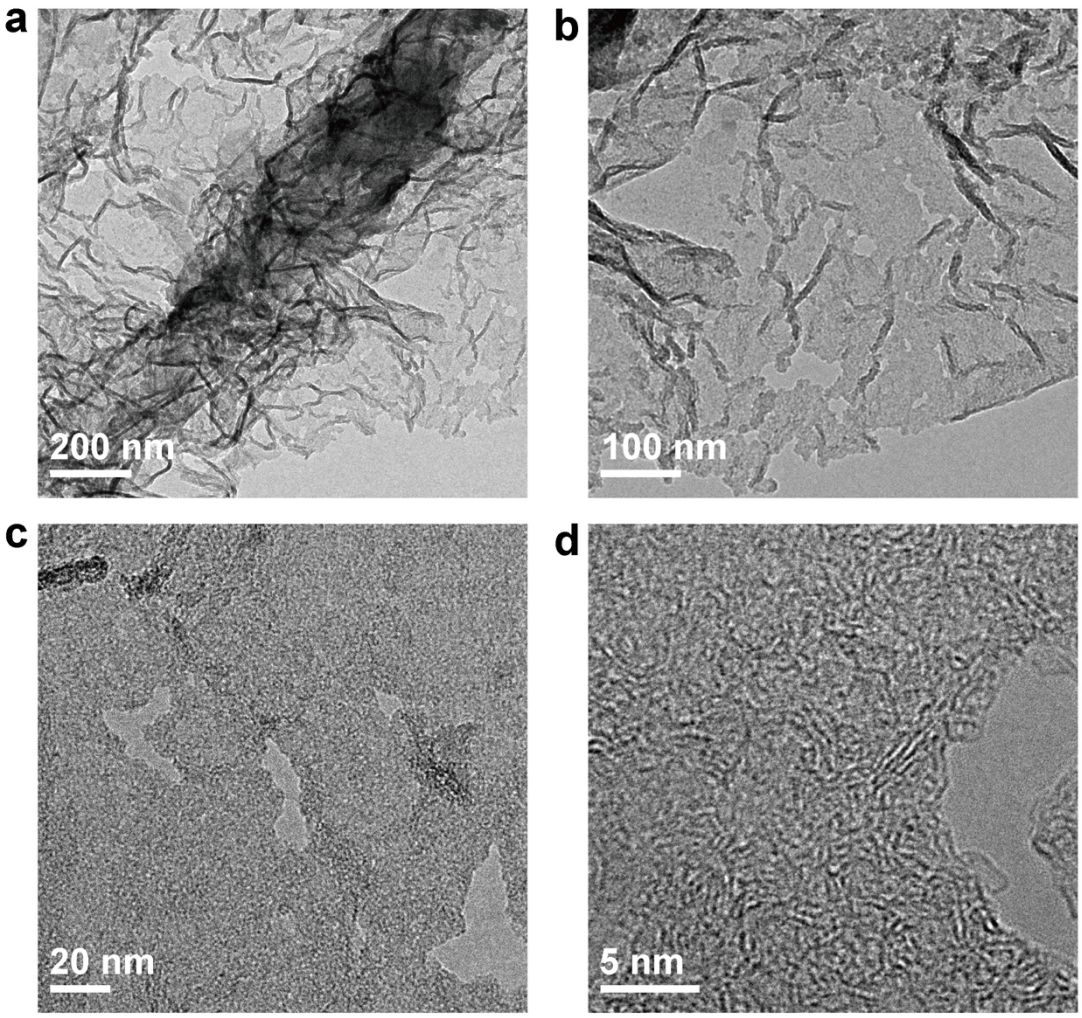

Fig. S9 (a-d) TEM images of MXene-derived inner carbon matrix.

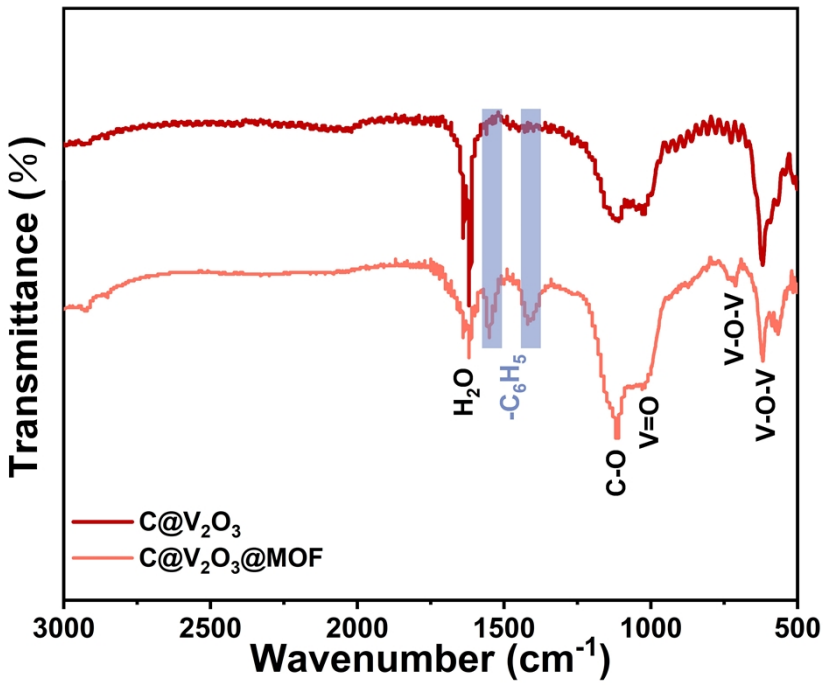

Fig. S10 FT-IR spectra of C@V_2O_3 and C@V_2O_3@MOF composites.

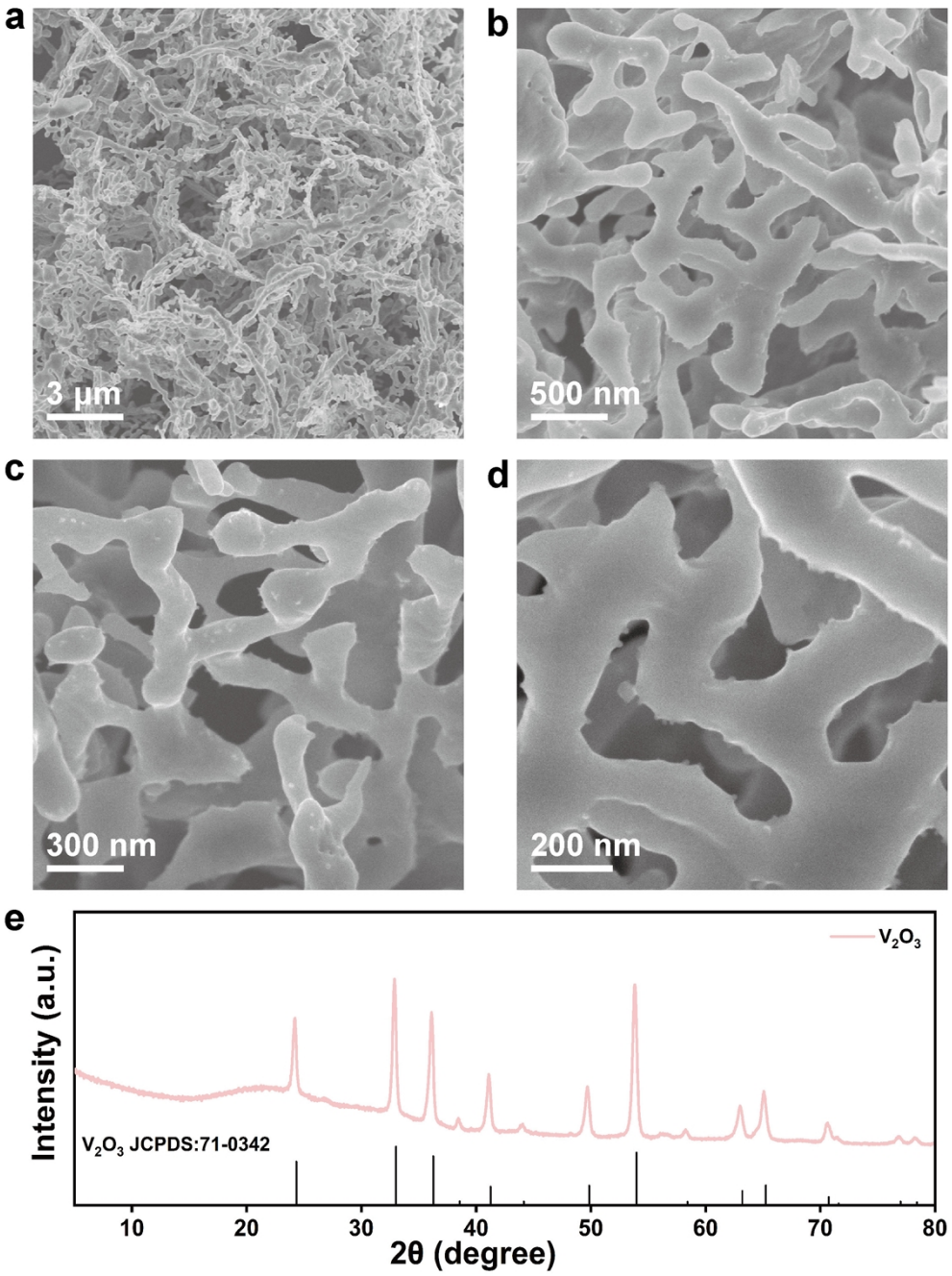

Fig. S11 (a-d) SEM images and (e) XRD profile of pure V_2O_3.

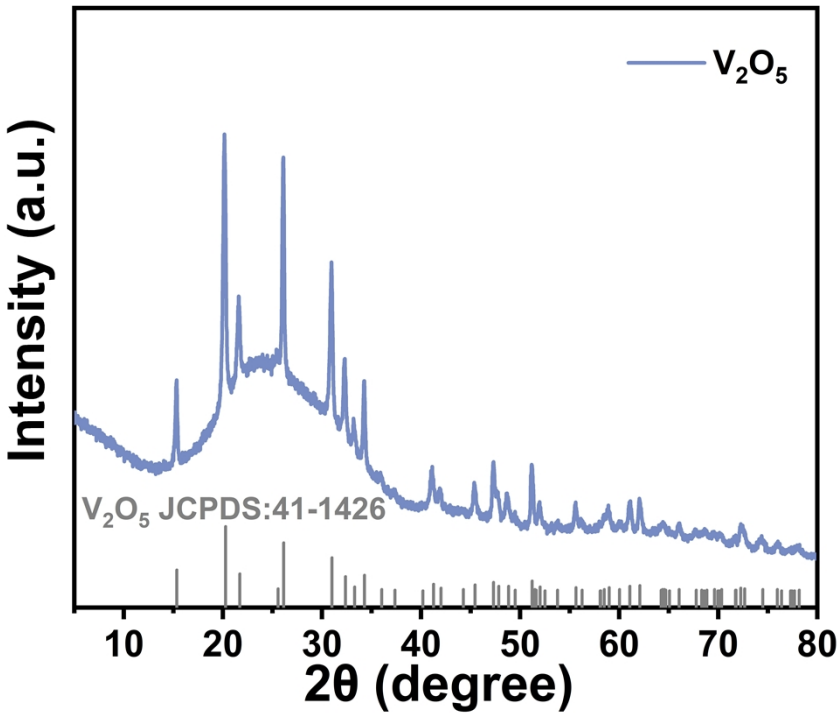

Fig. S12 XRD pattern of the final product after TGA test of C@V_2O_3@C composite in Air.

TGA calculation details: During TGA test, the carbon composition was oxidized to be gas. The oxidation product of C@V_2O_3@C after TGA test was characterized by XRD (Fig. S12), illustrating that the final product was V_2O_5. Therefore, the reaction equation of V_2O_3 during oxidation process was shown in Equation (1). The weight contents of V_2O_3 in C@V_2O_3 and C@V_2O_3@C composites were calculated to be 89.4 and 82 wt% based on Equation (2-3). Considering the weight ratio of V_2O_3 to inner MXene-carbon was 89.4: 10.6 in C@V_2O_3 composite, the weight contents of inner MXene-carbon and outer MOF-carbon in C@V_2O_3@C composite were determined to be 9.8 and 8.2 wt%, respectively.

$$V_2O_3 + O_2 = V_2O_5 \quad (1)$$

$$m_{V2O3}\ in\ C@V2O3 = \frac{m_{V2O5} \times M_{V2O3}}{M_{V2O5}} = \frac{108.4 \times 149.9}{181.9} = 89.4\ wt\% \quad (2)$$

$$m_{V2O3}\ in\ C@V2O3@C = \frac{m_{V2O5} \times M_{V2O3}}{M_{V2O5}} = \frac{99.6 \times 149.9}{181.9} = 82\ wt\% \quad (3)$$

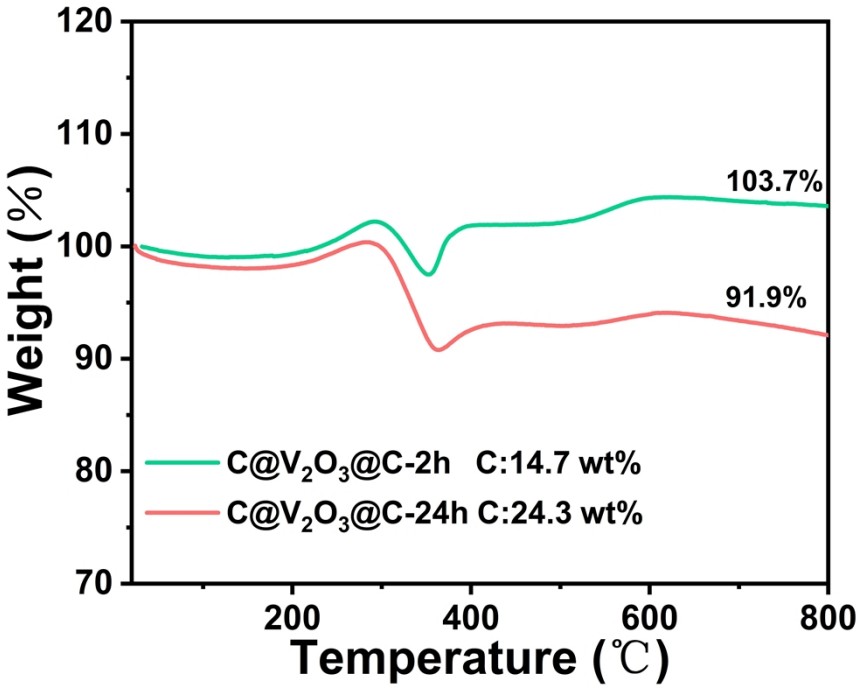

Fig. S13 TGA curves of C@V_2O_3@C-2h and C@V_2O_3@C-24h composites.

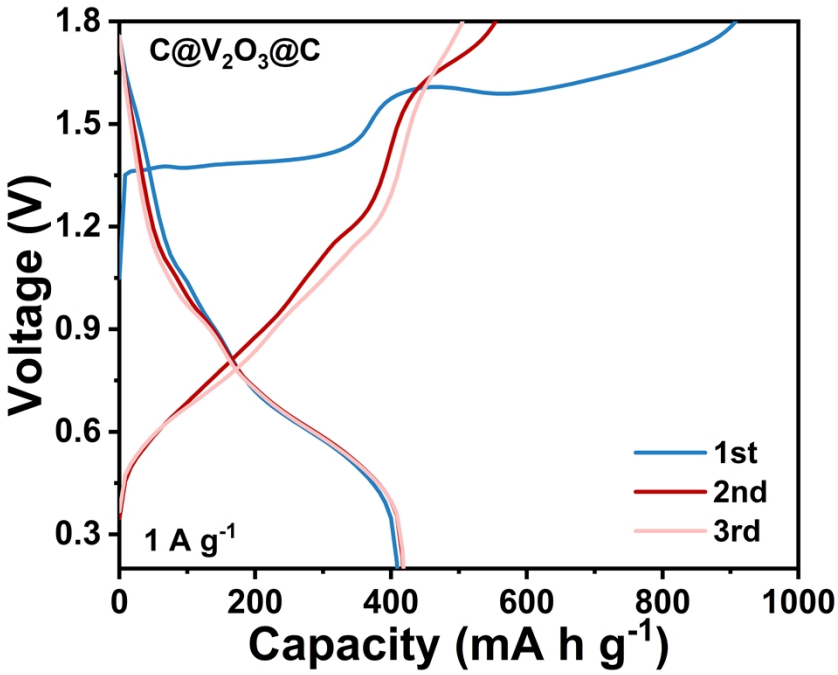

Fig. S14 Charge and discharge curves of C@V_2O_3@C at a current density of 1 A g^{-1}.

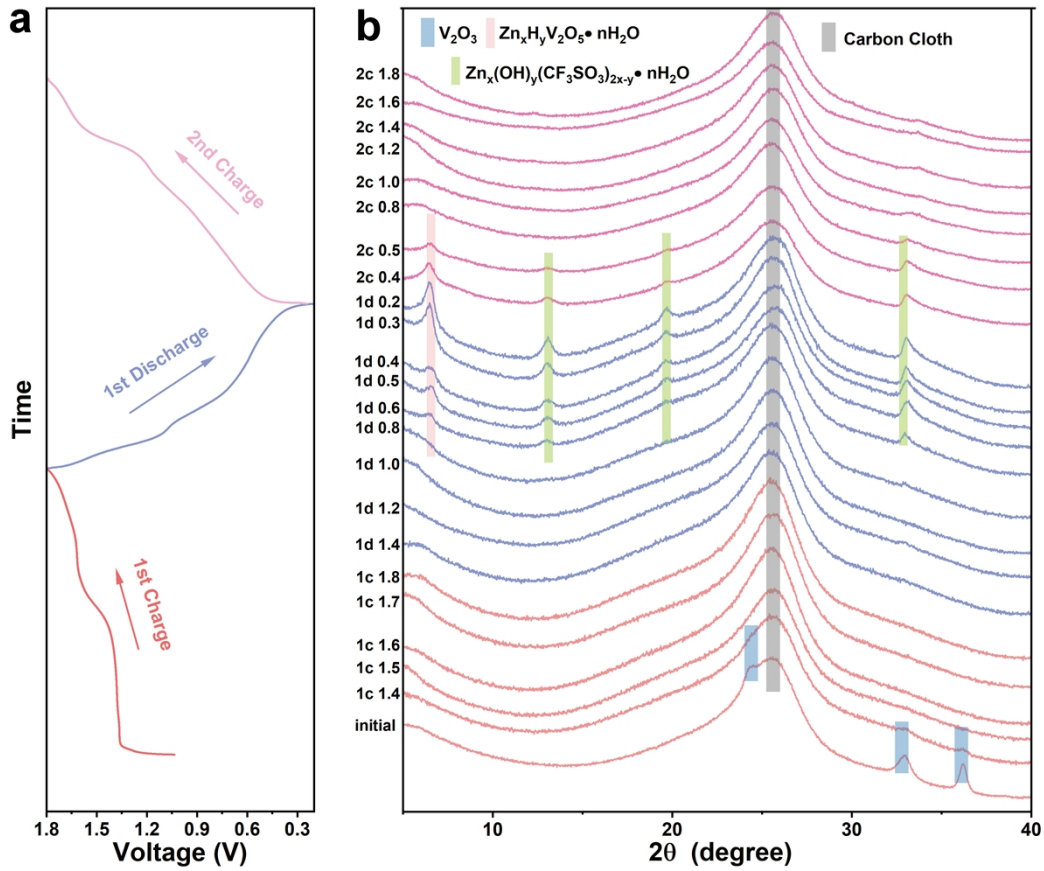

Fig. S15 (a) charge/discharge curves, and (b) *ex-situ* XRD profiles of C@V_2O_3@C under various states.

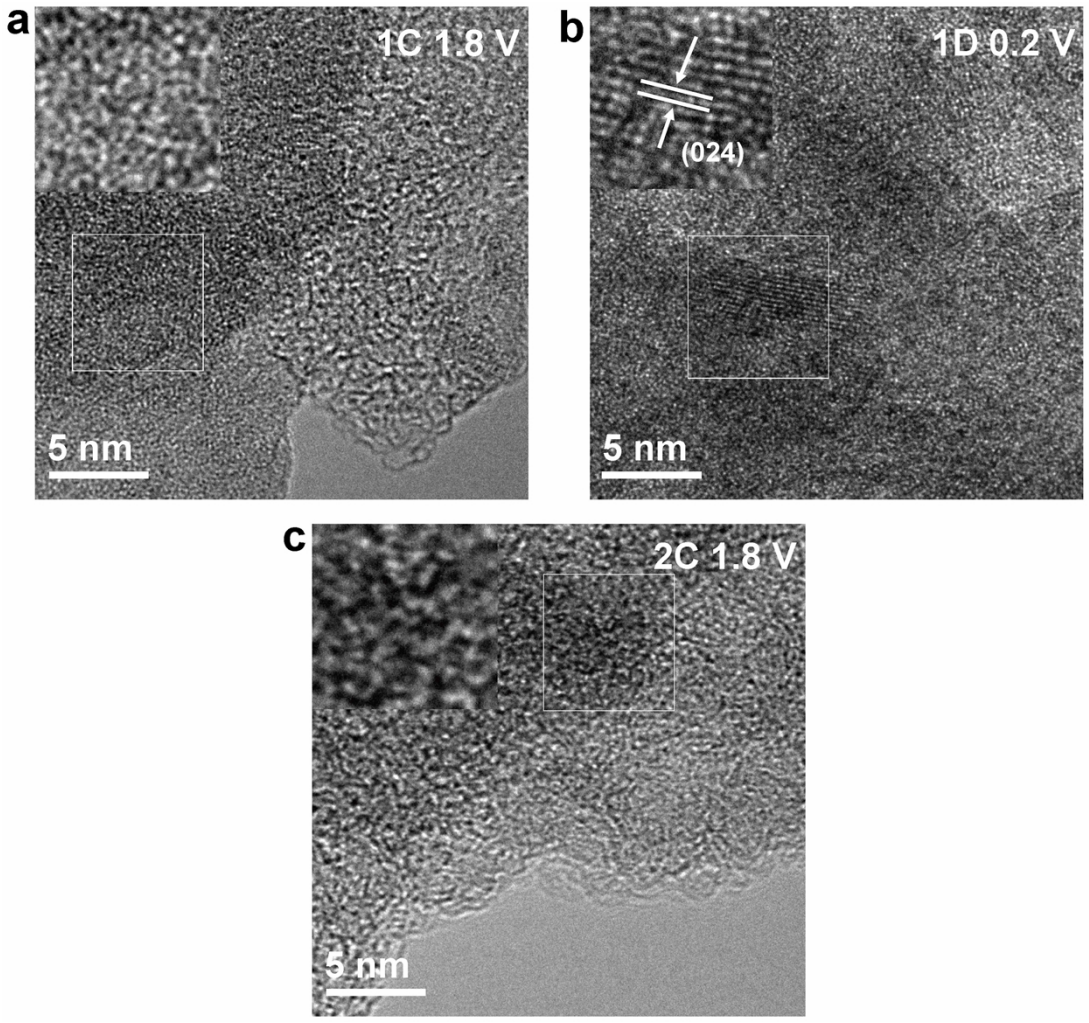

Fig. S16 *Ex-situ* TEM images of C@V_2O_3@C under various states at (a) 1st charge to 1.8 V, (b) 1st discharge to 0.2 V, and (c) 2nd charge to 1.8 V.

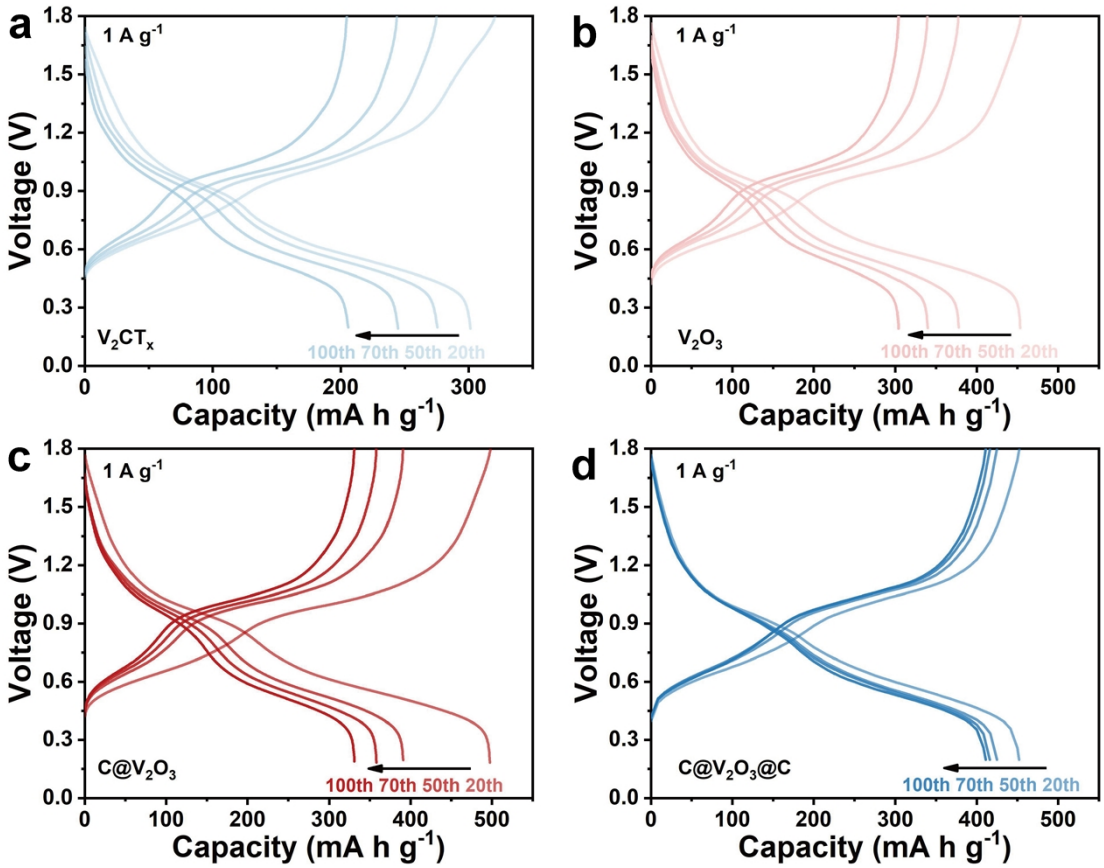

Fig. S17 Typical charge/discharge curves of (a) V_2CT_x, (b) V_2O_3, (c) C@V_2O_3, and (d) C@V_2O_3@C electrodes under various cycles at 1 A g^{-1}.

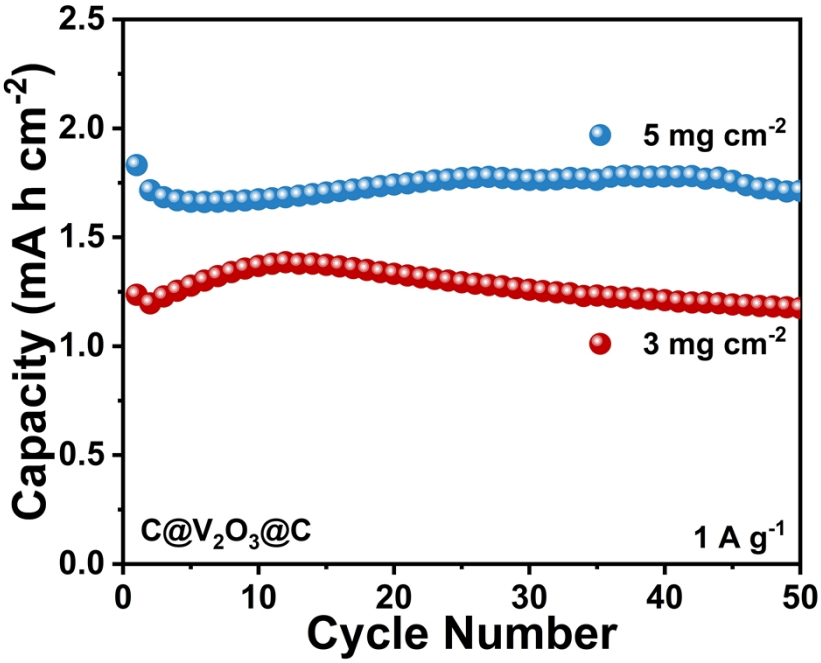

Fig S18 Cycling performance of C@V_2O_3@C electrodes under high loading mass of 3 and 5 mg cm^{-2} at 1 A g^{-1} for AZIBs.

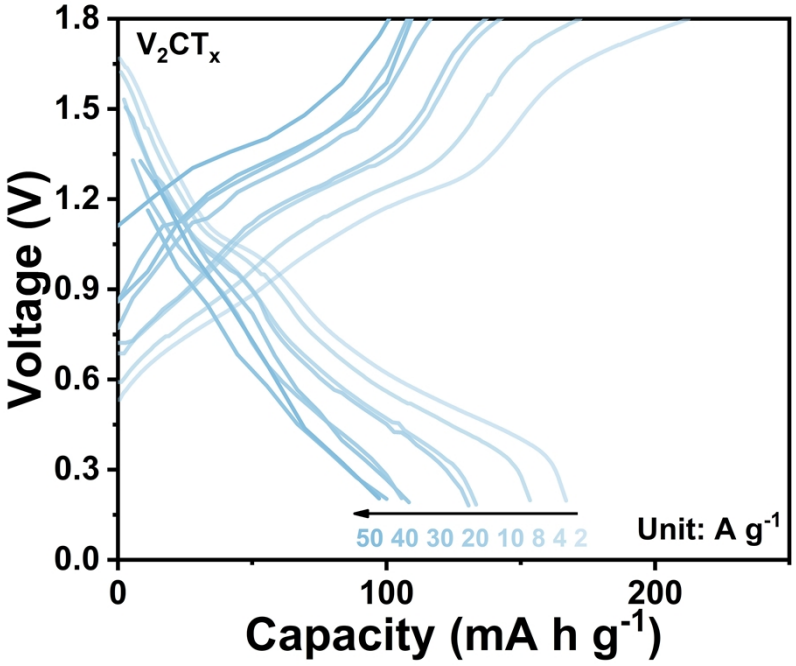

Fig. S19 Charge/discharge curves of V_2CT_x electrode at various rates from 2 to 50 A g^{-1}.

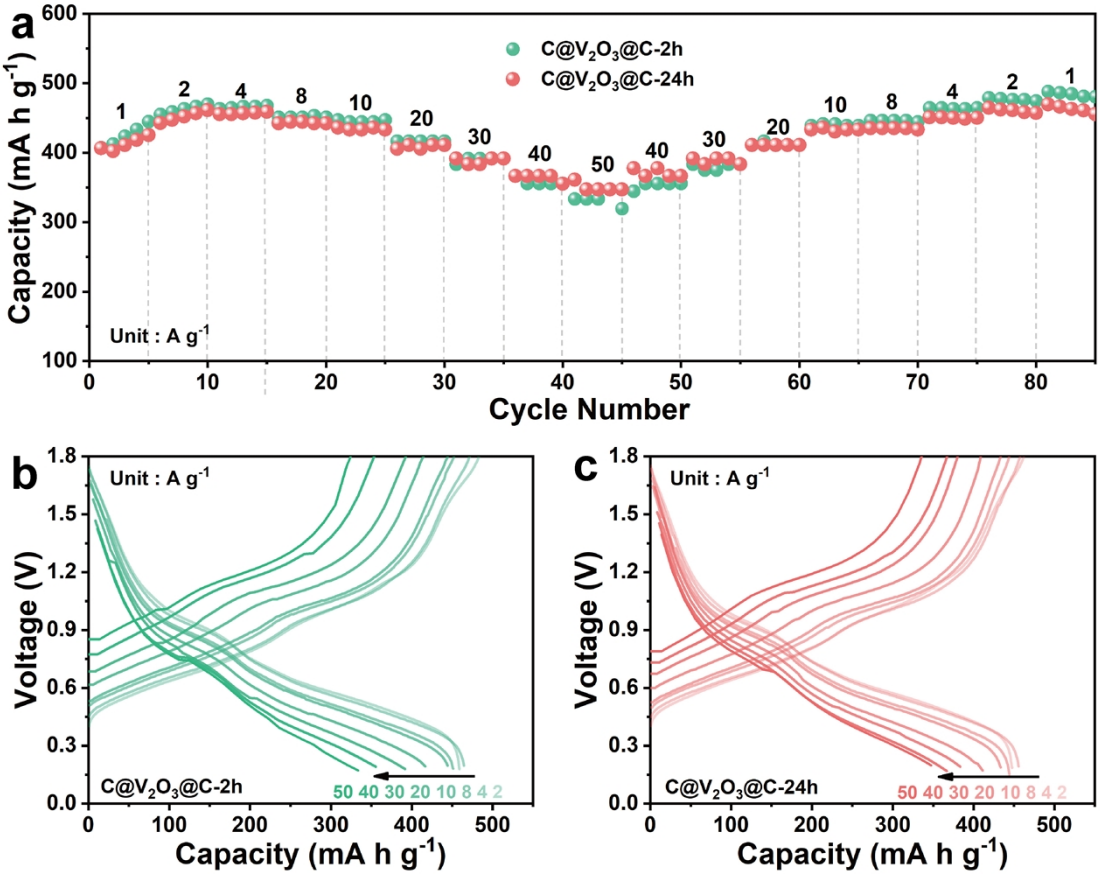

Fig. S20 (a) Rate performance from 2 to 50 A g^{-1}, and typical charge/discharge profiles under various current densities of (b) C@V_2O_3@C-2h and (c) C@V_2O_3@C-24h electrodes.

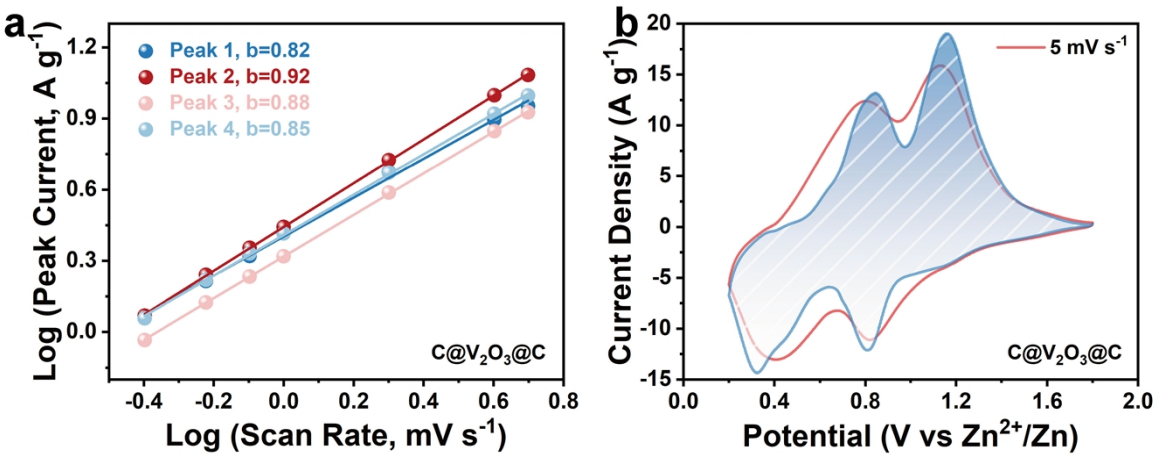

Fig. S21 (a) Log (i) versus log (v) plots and (b) CV curves showing the capacitive section at 5 mV s^{-1} of C@V_2O_3@C electrode.

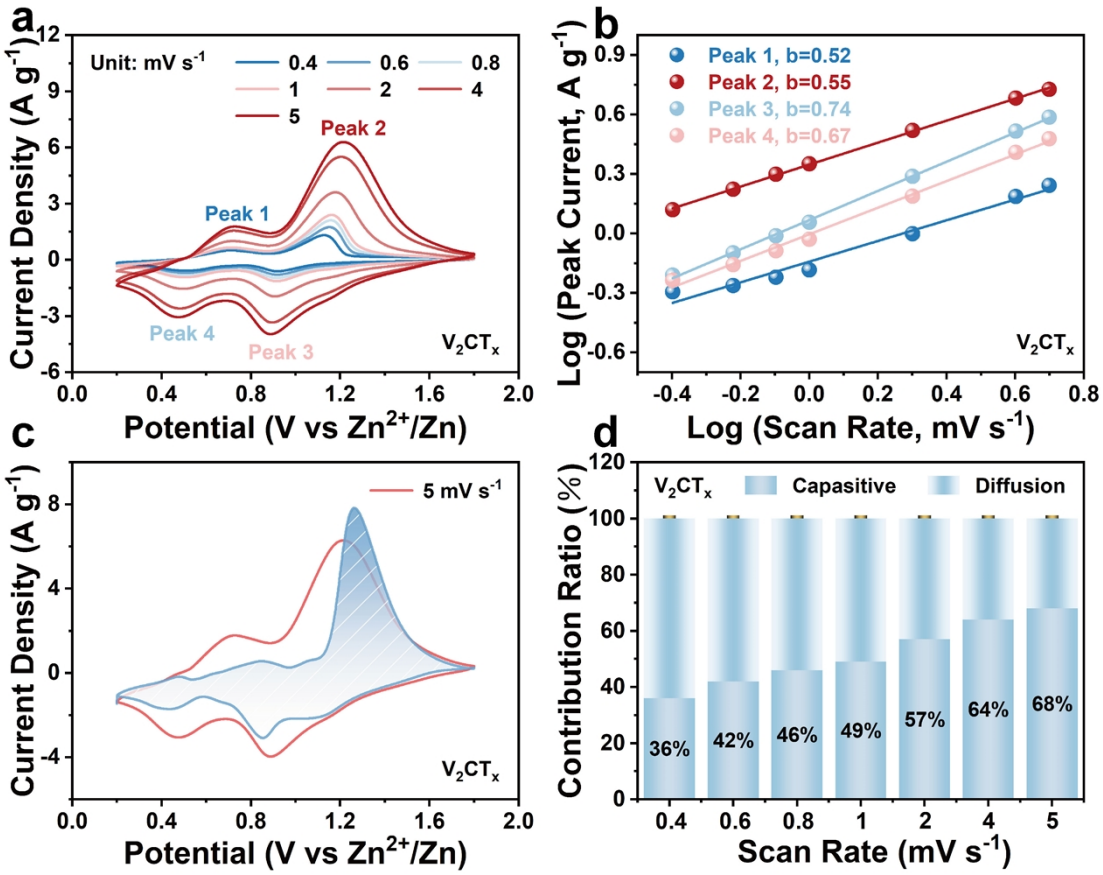

Fig. S22 (a) CV curves at different scan rates, (b) the corresponding Log (peak current) vs Log (scan rate) plots at each redox peak, (c) CV curves showing the capacitive section at 5 mV s^{-1}, and (d) capacitive and diffusion contribution at different scan rates of V_2CT_x cathode.

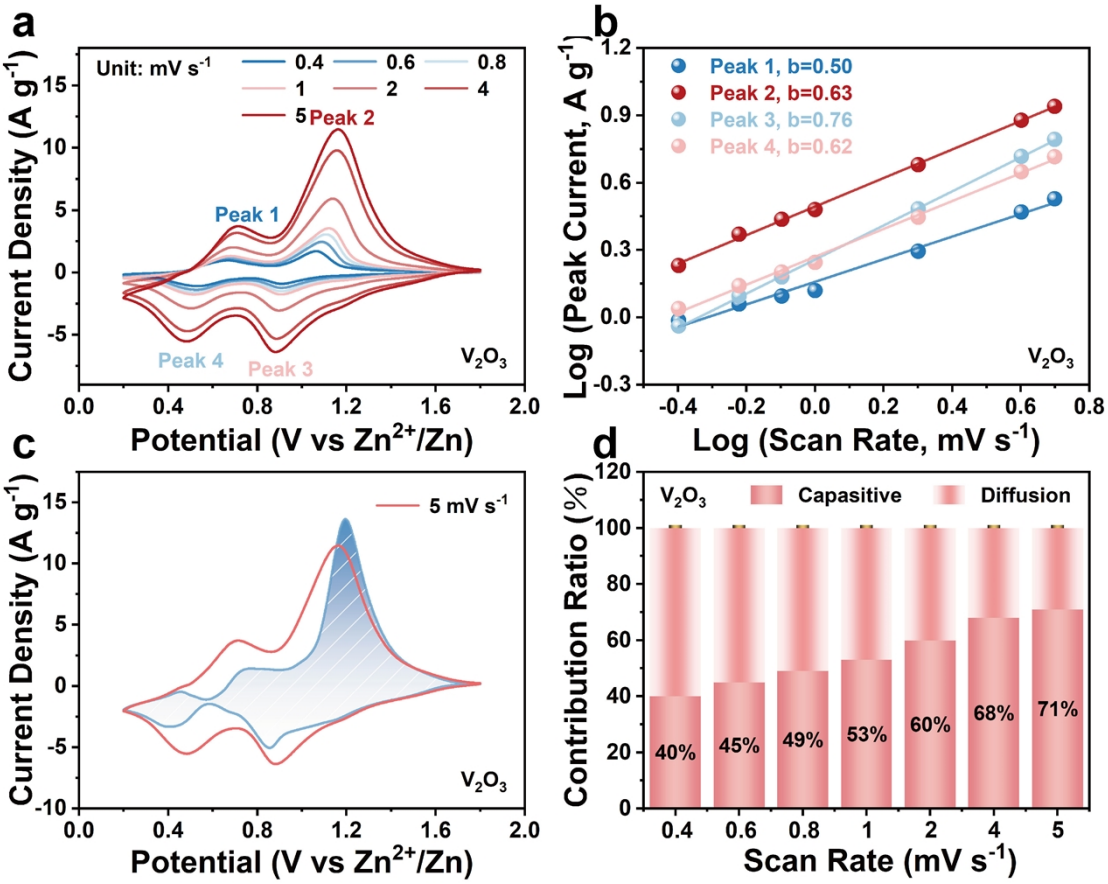

Fig. S23 (a) CV curves at different scan rates, (b) the corresponding Log (peak current) vs Log (scan rate) plots at each redox peak, (c) CV curves showing the capacitive section at 5 mV s^{-1}, and (d) capacitive and diffusion contribution at different scan rates of V_2O_3 cathode.

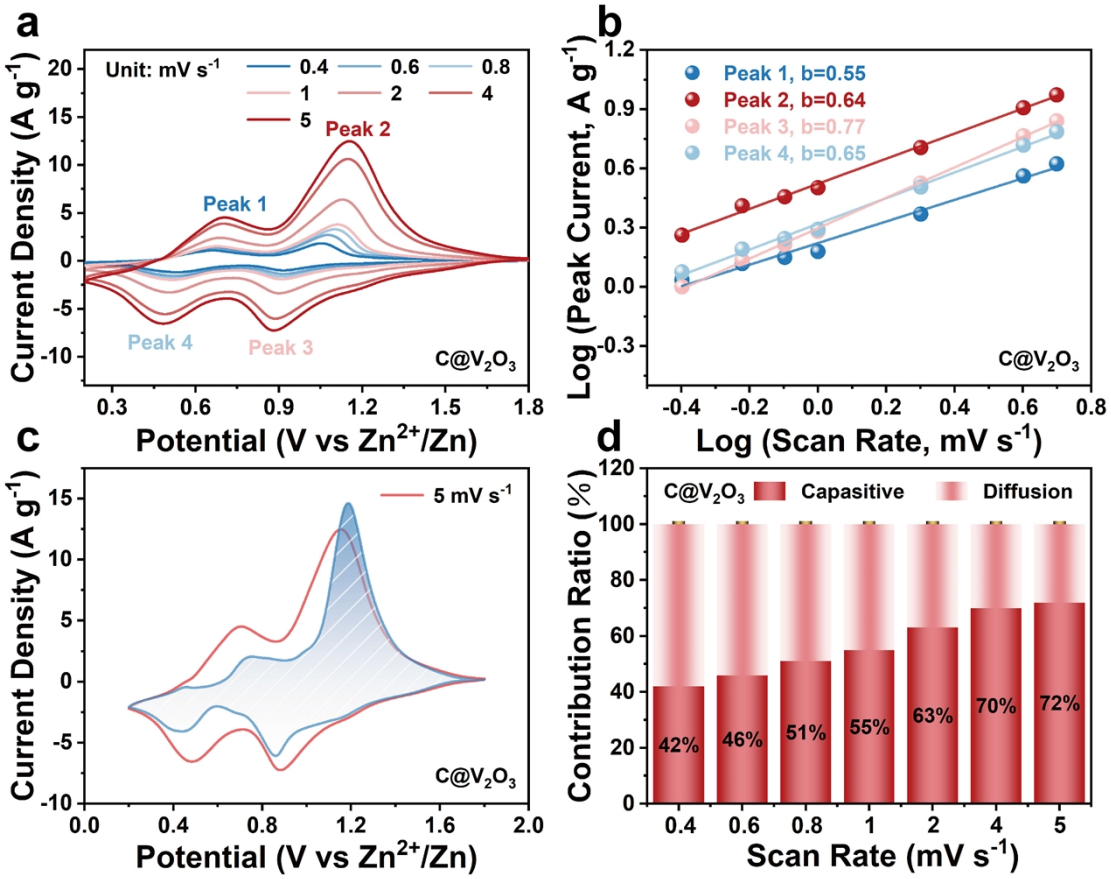

Fig. S24 (a) CV curves at different scan rates, (b) the corresponding Log (peak current) vs Log (scan rate) plots at each redox peak, (c) CV curves showing the capacitive section at 5 mV s^{-1}, and (d) capacitive and diffusion contribution at different scan rates of C@V_2O_3 cathode.

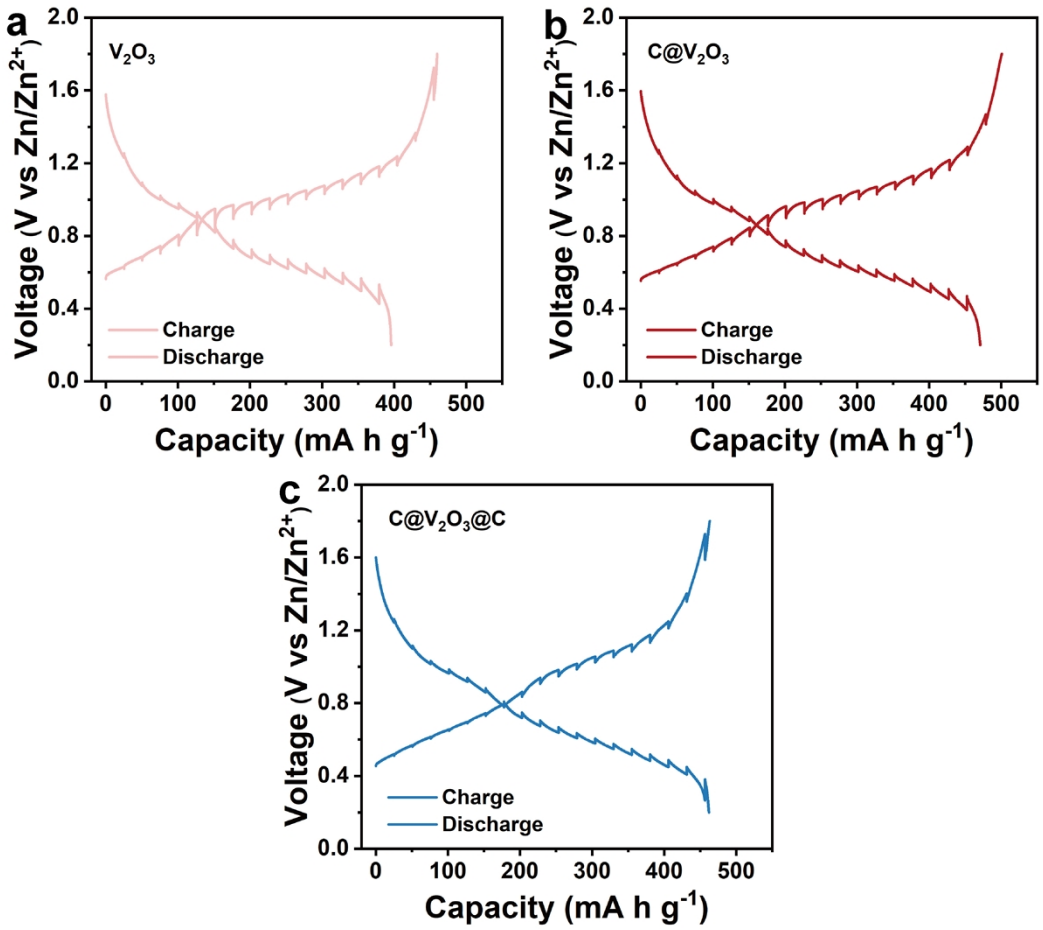

Fig. S25 GITT curves of (a) V_2O_3, (b) C@V_2O_3, and (c) C@V_2O_3@C electrodes at 10th cycle, which were recorded under current pluses of 50 mA g^{-1} for 30 min and relaxation of 2 h at each interval.

GITT calculation details: The ion diffusion coefficient (D_{ion}) can be quantitatively calculated based on the simplified Fick's second law (Equation (4)):[8-10]

$$D_{ion} = \frac{4}{\pi\tau}\left(\frac{m_B V_m}{M_B A}\right)^2\left(\frac{\Delta E_s}{\Delta E_\tau}\right)^2 \quad (4)$$

Where V_m, M_B, and m_B are the molar volume, the molecular weight, and the mass of the compound, respectively. A is the geometric area of the electrode. ΔE_s and ΔE_τ are the voltage changes during the time period τ (30 min) and after 2 h of open-circuit stand. As can be seen, carbon matrix can significantly enhance the ion-diffusion ability of V_2O_3 cathode. As a result, dual-carbon protected C@V_2O_3@C exhibited the highest D_{ion} with an average value of 2.7×10^{-11} cm^2 s^{-1} during 10th cycle, much higher than that of 0.99×10^{-11} and 0.75×10^{-11} cm^2 s^{-1} for C@V_2O_3 and V_2O_3 electrodes.

a

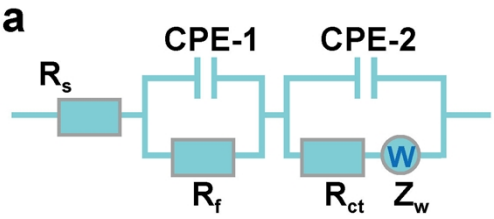

b

Electrode	R_{ct} (Ω)
$C@V_2O_3@C$	20.5
$C@V_2O_3$	43.7
V_2O_3	73.1

Fig S26 (a) The equivalent circuit model and (b) the simulated R_{ct} values of $C@V_2O_3@C$, $C@V_2O_3$, and V_2O_3 electrodes.

The Nyquist plots of $C@V_2O_3@C$, $C@V_2O_3$, and V_2O_3 electrodes after 20 cycles are fitted with an equivalent circuit model in Fig. S26, where R_s, R_f, and R_{ct} represent the total ohmic resistance of the electrode system, the diffusion resistance of ions through SEI film in the high-frequency region, and the charge-transfer resistance in the middle-frequency region, respectively. Z_w is the Warburg impedance for ion diffusion in the active material related with the slant line in low-frequency region. CPE-1 and CPE-2 are related to the surface capacitance and double layer capacitance, respectively.

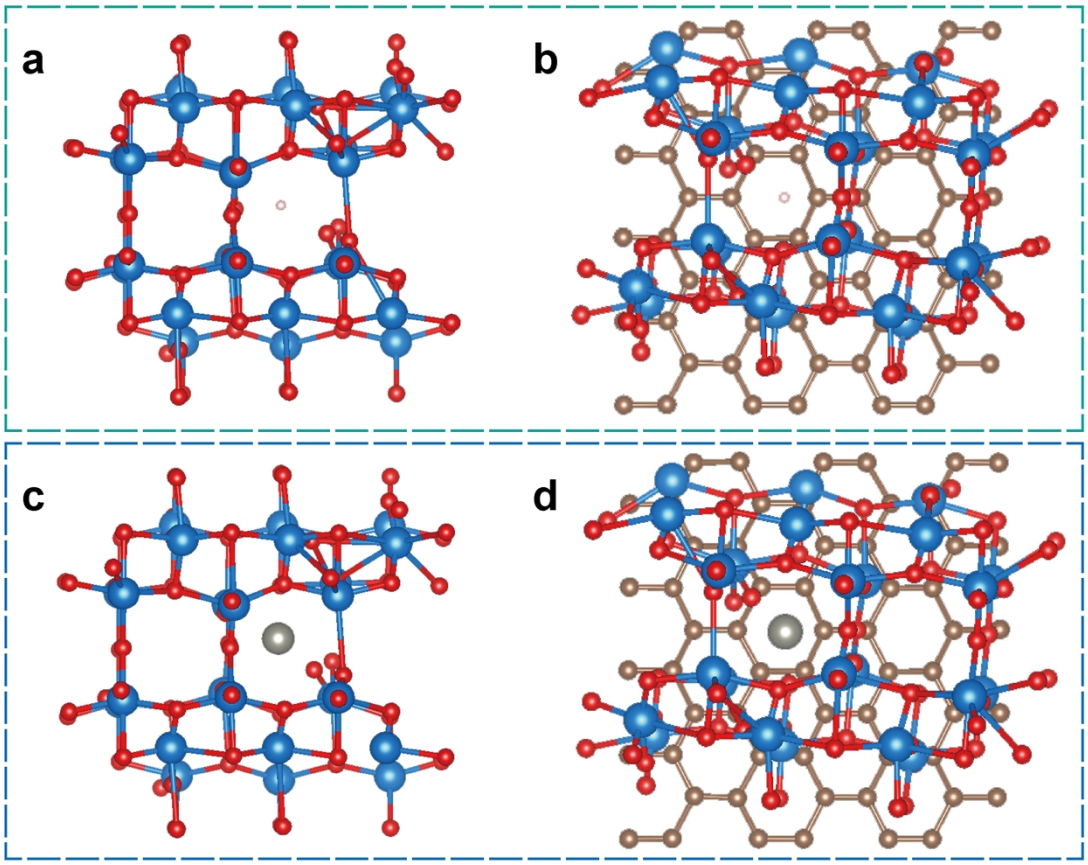

Fig. S27 Top views of (a-b) H-ion and (c-d) Zn-ion adsorption on (a, c) a-VO_x and (b, d) a-VO_x/C interface.

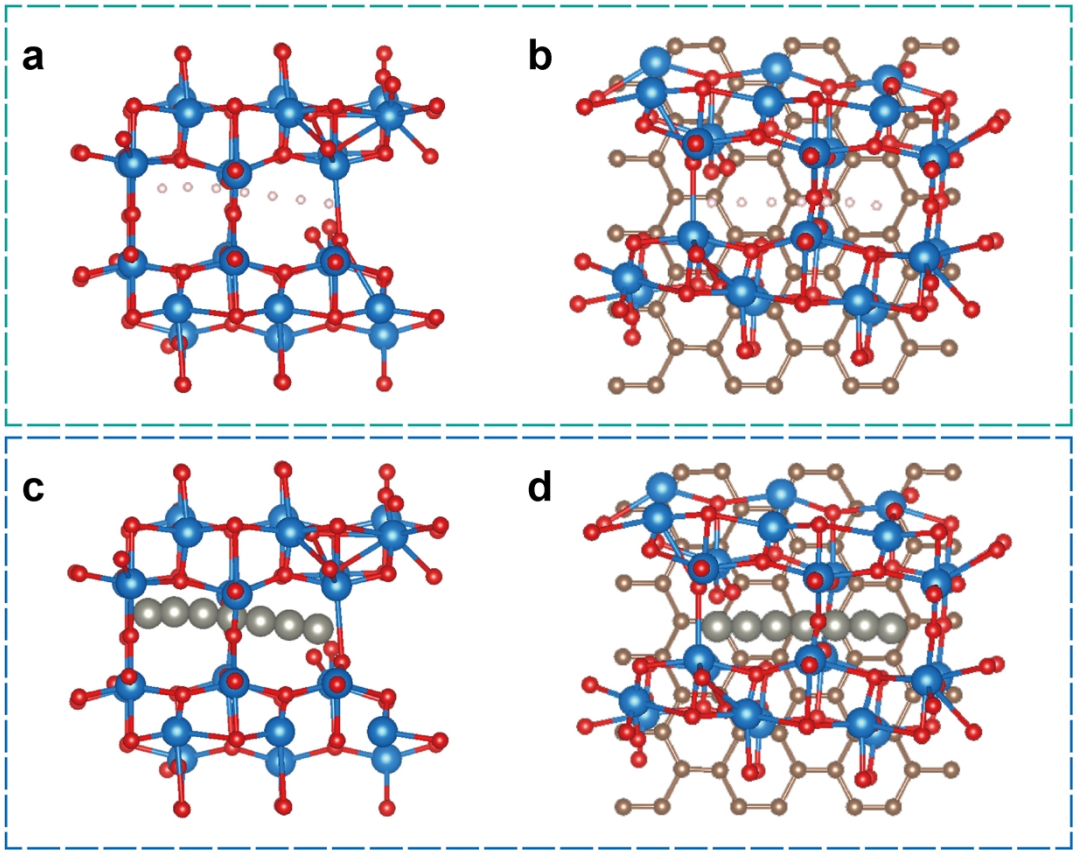

Fig. S28 Top views of (a-b) H-ion and (c-d) migration paths on (a, c) a-VO_x and (b, d) a-VO_x/C interface.

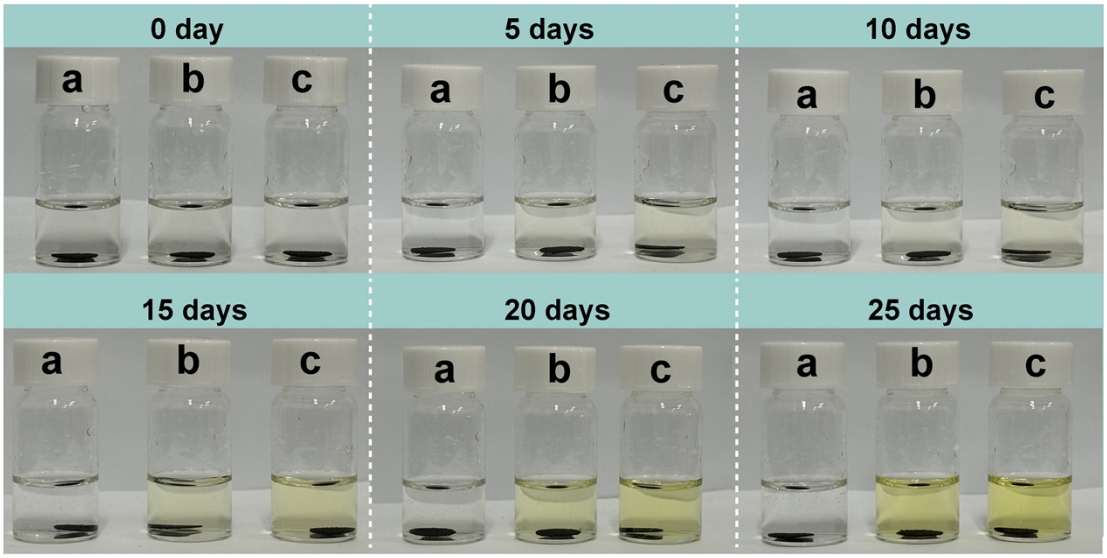

Fig. S29 Photos of the V-dissolution tests by immersing (a) C@V_2O_3@C, (b) C@V_2O_3 and (c) V_2O_3 electrodes in 3M $Zn(CF_3SO_3)_2$ electrolytes for different soaking time.

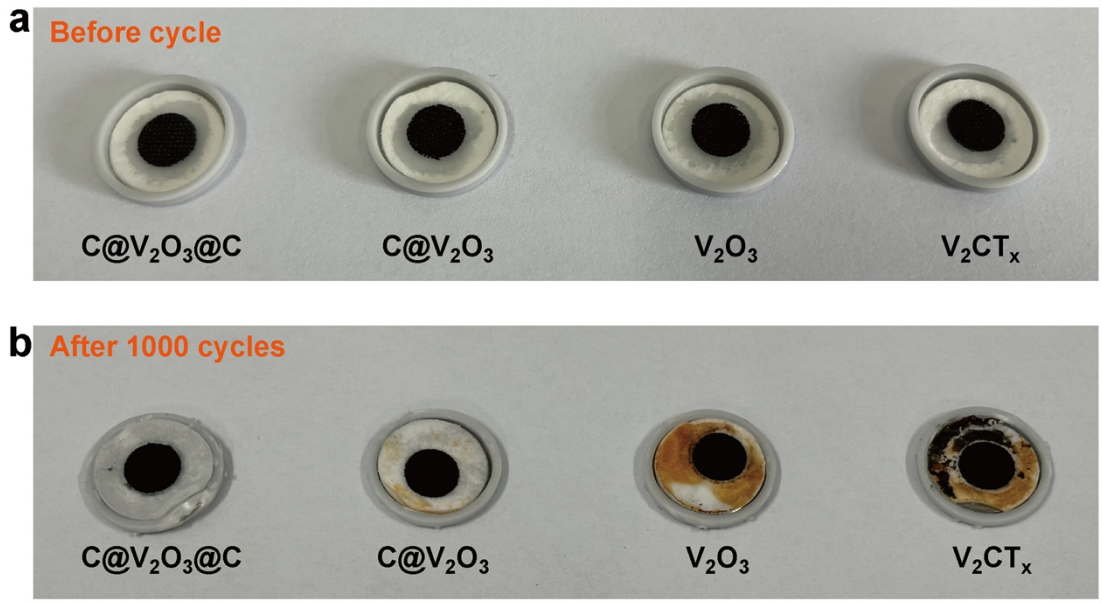

Fig. S30 Photos showing the color changes of glass fiber membranes for $C@V_2O_3@C$, $C@V_2O_3$, V_2O_3 and V_2CT_x cathodes (a) before and (b) after 1000 cycles at 30 A g^{-1}.

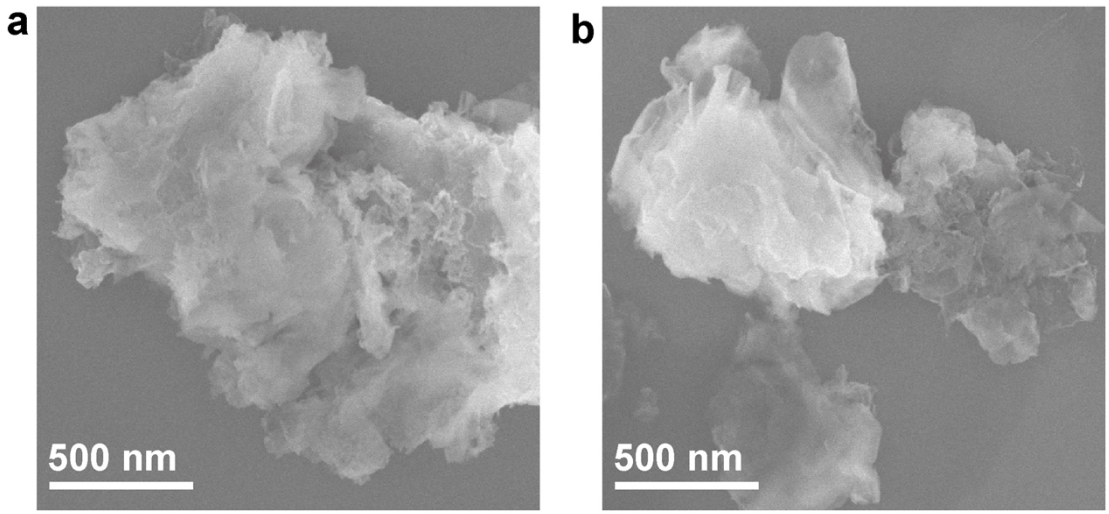

Fig. S31 (a-b) SEM images of C@V_2O_3@C after 1000 cycles.

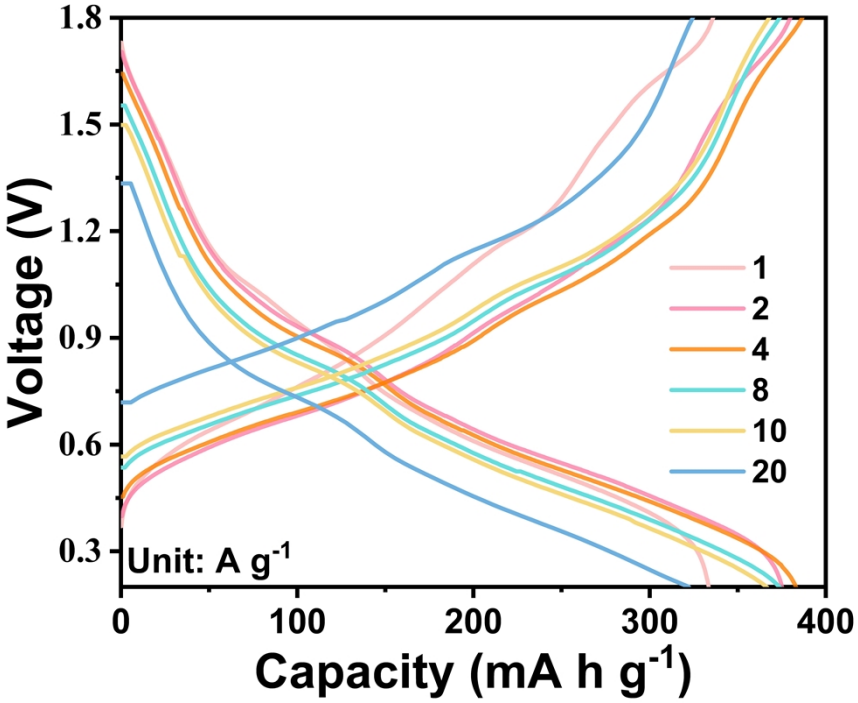

Fig. S32 Charge and discharge curves of C@V_2O_3@C constructed quasi solid-state ZIBs at different current densities from 1 to 20 A g^{-1}.

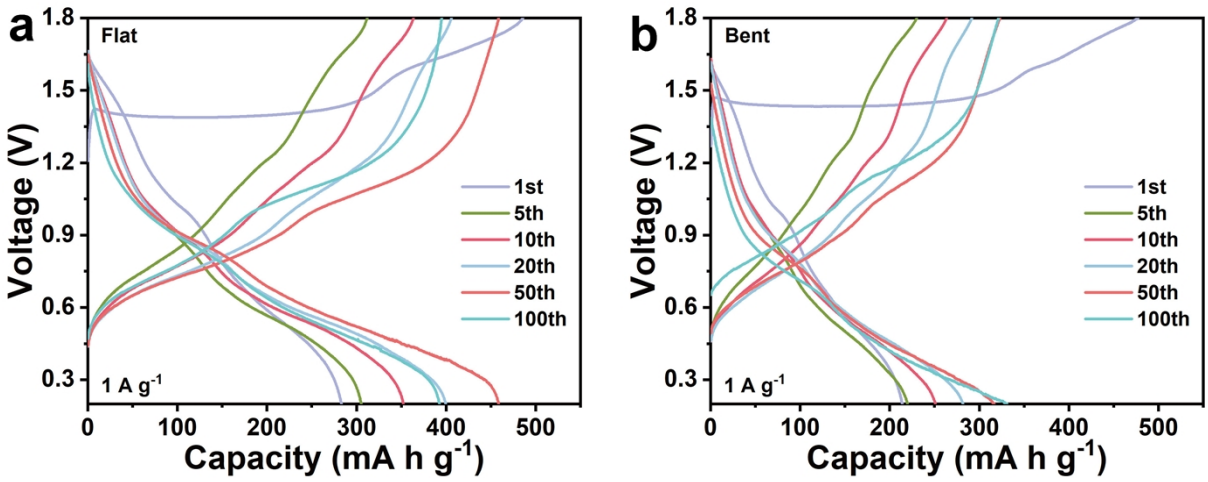

Fig. S33 Charge and discharge curves of C@V_2O_3@C constructed quasi solid-state ZIBs at 1 A g^{-1} under (a) flat and (b) bent states.

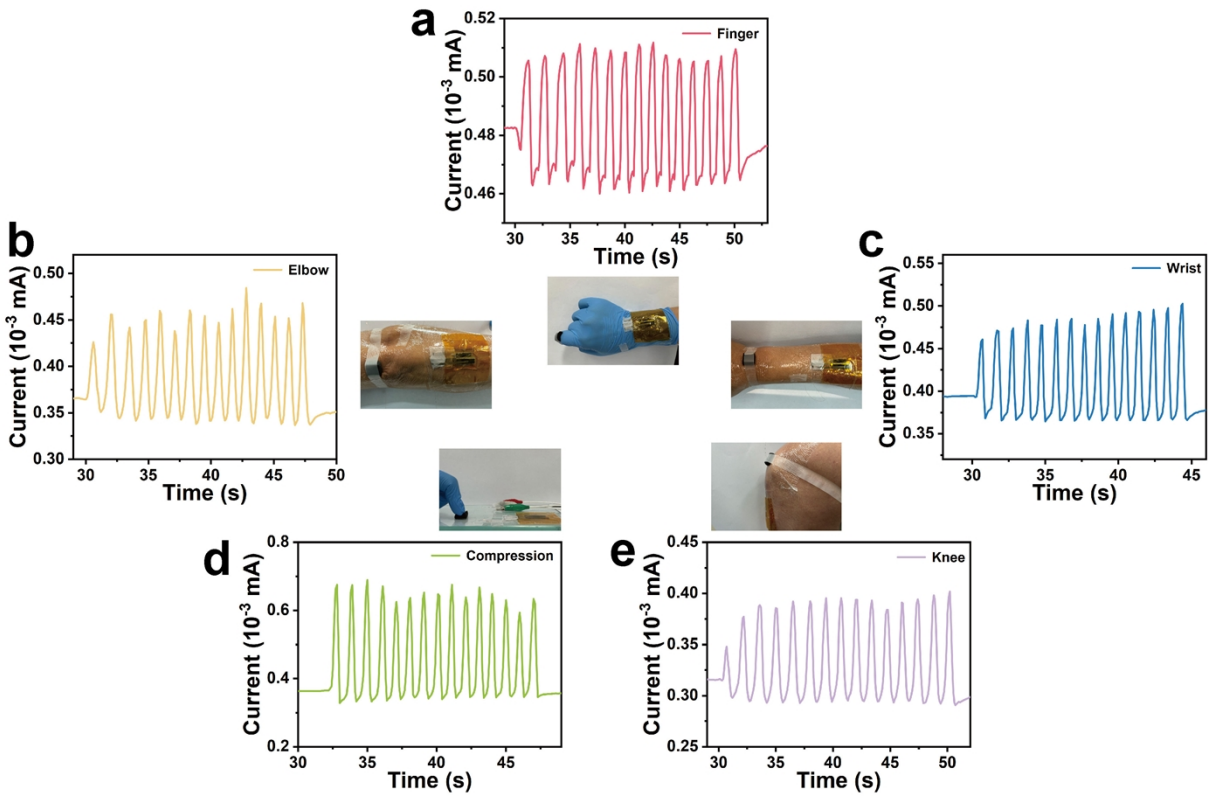

Fig. S34 A self-powered wearable system consisted of flexible ZIBs and a flexible pressure sensor for monitoring real-time human motion of (a) finger, (b) elbow, (c) wrist, (d) finger compression, and (e) knee.

Table S1. Comparison of rate performance between C@V_2O_3@C and as-reported vanadium-based materials in AZIBs.

Materials	**Current Density (A g^{-1})/Cycle Number**	**Capacity retention ratio (%)**	**Rate (mA h g^{-1}/A g^{-1})**	**Rate (mA h g^{-1}/A g^{-1})**	**Loading mass (mg cm^{-2})**	**References**
V_2O_3-SP2	0.5/20	100	325.2/5	264.6/10	-	11
NVO-AVO	-	-	221.4/4	204.9/5	-	12
Tau-VOP	0.2/50	94	110/4	104/5	1.3	13
LEF-VO	0.2/120	91	345/10	283.5/20	1.5	14
CaNaVO-44@Cs	0.2/100	89	221.4/5	196.1/10	5	15
VO_2-A	0.5/200	80.7	374.4/5	357/10	~1	16
PEO-LVO	0.3/100	97.3	328.4/15	302.4/20	24	17
RuVO	0.2/200	87	248.3/10	180.6/20	1	18
V_2O_3@CSs	2/300	90	216/20	229/18	~1.5	19
VO@NDA	2/1800	100	258/8	241/10	-	20
V_2C/V_2O_5	-	-	280/20	232/25	1.0-1.5	21
LNVO	-	-	350/40	320/50	4.5	22
C@V_2O_3@C	**1/100**	**100**	**411/40**	**402/50**	**1.2-1.6**	**This work**

Table S2. Comparison of cycling performance between C@V_2O_3@C cathode and other vanadium oxide, vanadium sulfide, manganese oxide, and Prussian blue analog cathodes in AZIBs.

Materials	Current Density (A g^{-1})	Cycle Number	Capacity remained (mA h g^{-1})	Rate (mA h g^{-1}/A g^{-1})	Loading mass (mg cm^{-2})	References
T-HVO|O_d	10	1000	275	217.7/30	1-2	23
CoVO@$PANI_{60}$	10	1500	200	140.8/10	1	24
p-VON@C	10	2000	265	296/10	2	25
V_2O_3-SP2	10	2000	235	264.6/10	-	11
VO_2	20	2000	194	272/20	2	26
V_2O_3@CSs	10	3000	150	216/20	~1.5	19
VOOH/VS_x	10	700	235	243/10	1.8-2.3	27
VS_2-M	3	900	101	150.5/2	1.27-2.55	28
ZnV_2S_4	4	1000	246	230/8	0.8-1.4	29
SL-VS_2@CS	8	1000	218.2	206.5/8	-	30
$VS_2 \perp V_4C_3T_x$	5	2000	155	143.2/20	-	31
Co-$VS_{4-\delta}$-0.03	5	3000	160	270.7/5	0.66	32
δ -MnO_2	3	1000	150	141/3	-	33
$Al_{0.05}$-MnO_2	1	1000	130	135.8/8	1.5	34
$Ce_{in/inter}$-MnO_2	3	2000	150	140.5/3	1-2	35
BiO-MnO_2	2	2000	140	204.5/4	1-2	36
KMO-NAPD	4	2000	75	70/8	-	37
Mn-PBA-3	10	2000	86	149.5/3	1	38
V-PBA	2	2000	70	27.6/10	0.5-0.8	39
C@V_2O_3@C	**30**	**3000**	**240**	**441/10 402/50**	**1.2-1.6**	**This work**

Table S3. Comparison of the rate performance between C@V_2O_3@C and other vanadium oxide cathodes for flexible quasi solid-state ZIBs.

Materials	**Rate (mA h g^{-1}/A g^{-1})**	**References**
V_2CT_x	164.5/20	40
NaNVO-PANI@CC	136.6/8	41
AVSO@CC	160/20	42
DMF-NVO NFAs/CC	212/5	43
H-V_2O_5	121/30	44
V_2O_5@C	117.5/20	45
$H_2V_3O_8$	170/10	46
NVO_2/CNT	193.6/10	47
VS_2@CF	148.9/5	48
NVO	170/5	49
C@V_2O_3@C	**320/20**	**This Work**

References

1. M. Naguib, R. R. Unocic, B. L. Armstrong and J. Nanda, *Dalton Trans.*, 2015, **44**, 9353-9358.
2. G. Kresse and J. Furthmüller, *Phys. Rev. B*, 1996, **54**, 11169–11186.
3. J. P. Perdew, K. Burke and M. Ernzerhof, *Phys. Rev. Lett.*, 1996, **77**, 3865–3868.
4. G. Kresse and D. Joubert, *Phys. Rev. B*, 1999, **59**, 1758-1775.
5. P. E. Blöchl, *Phys. Rev. B*, 1994, **50**, 17953-17979.
6. S. Grimme, J. Antony, S. Ehrlich and H. Krieg, *H. J. Chem. Phys.*, 2010, **132**, 154104.
7. G. Henkelman, B. P. Uberuaga and H. Jónsson, *H. J. Chem. Phys.*, 2000, **113**, 9901-9904.
8. H. Luo, B. Wang, F. Wang, J. Yang, F. Wu, Y. Ning, Y. Zhou, D. Wang, H. Liu and S. Dou, *ACS Nano*, 2020, **14**, 7328-7337.
9. Q. Yao, Y. Gan, Z. Ma, X. Qian, S. Cai, Y. Zhao, L. Guan and W. Huang, *Energy Environ. Mater.*, 2022, **5**, 944-953.
10. Y. Liu, T. Wang, Y. Sun, M. Zhang, G. Gao, J. Yang and K. Cai, *Chem. Eng. J.*, 2024, **484**, 149501.
11. D. Li, Z. Ye, H. Ding, J. Li, H. Huang, Z. Yang, J. Su, J. Zhu and W. Zhang, *Energy Stor. Mater.*, 2024, **71**, 103635.
12. L. Xing, X. Zhang, N. Xu, P. Hu, K. Wang and Q. An, *Adv. Funct. Mater.*, 2024, **34**, 2312773.
13. Q. Jiang, W. Zhao, S. Wang, W. Wu, H.-Y. Shi, X.-X. Liu and X. Sun, *Energy Stor. Mater.*, 2024, **70**, 103494.
14. H. Liu, X. Hou, S. Fan, M. Cen, Z. Chen, B. Chen, C. Yuan, W. Peng, Y. Li and X. Fan, *Adv. Energy Mater.*, 2024, 2402416.
15. C. Zhang, Y. Huang, X. Xu, Z. Chen, G. Xiao, Y. Zhong, X. Wang, C. Gu and J. Tu, *Energy Environ. Sci.*, 2024, **17**, 4090-4103.
16. Q. He, T. Hu, Q. Wu, C. Wang, X. Han, Z. Chen, Y. Zhu, J. Chen, Y. Zhang, L. Shi, X. Wang, Y. Ma and J. Zhao, *Adv. Mater.*, 2024, **36**, 2400888.
17. M. Wu, C. Shi, J. Yang, Y. Zong, Y. Chen, Z. Ren, Y. Zhao, Z. Li, W. Zhang, L. Wang, X. Huang, W. Wen, X. Li, X. Ning, X. Ren and D. Zhu, *Adv. Mater.*, 2024, **36**, 2310434.
18. Z. Chen, H. Liu, S. Fan, Q. Zhang, C. Yuan, W. Peng, Y. Li and X. Fan, *Adv. Energy*

Mater., 2024, **14**, 2400977.

19. Y. Zhao, T. He, J. Li, C. Zhu, Y. Tan, K. Zhu, S. Chou and Y. Chen, *Angew. Chem. Int. Ed.*, 2024, **63**, e202408218.
20. Z. Song, Y. Zhao, H. Wang, A. Zhou, X. Jin, Y. Huang, L. Li, F. Wu and R. Chen, *Energy Environ. Sci.*, 2024, **17**, 6666-6675.
21. P. Cai, K. Wang, X. He, Q. Li, Z. Zhang, M. Li, H. Li, M. Zhou, W. Wang and K. Jiang, *Energy Stor. Mater.*, 2023, **60**, 102835.
22. B. Liu, A. Huang, X. Yuan, X. Chang, Z. Yang, K. Lyle, R. B. Kaner and Y. Li, *Adv. Mater.*, 2024, **36**, 2404796.
23. J. Chen, Y. Liu, B. Xiao, J. Huang, H. Chen, K. Zhu, J. Zhang, G. Cao, G. He, J. Ma and S. Peng, *Angew. Chem. Int. Ed.*, 2024, **63**, e202408667.
24. X.-W. Liang, Y.-Y. Yang, W.-F. Di, S.-Y. Chen, R. Zhang, J. Hu, D. Lin and Y. Huo, *Chem. Eng. J.*, 2024, **495**, 153255.
25. Y. Liu, J. Zhang, Y. Liu, M. Zhang, Z. Pan and K. Cai, *Small*, 2024, **20**, 2401922.
26. W. Deng, Z. Xu, G. Li and X. Wang, *Small*, 2023, **19**, 2207754.
27. Y. Liu, Y. Sun, J. Zhang, X. Hao, M. Zhang, P. Wei, X. Zhao and K. Cai, *Nano Energy*, 2024, **120**, 109152.
28. T. Wang, W. Gao, Y. Zhao, S. Wang and W. Huang, *J. Mater. Sci. Technol.*, 2024, **173**, 107-113.
29. M. Narayanasamy, B. Balan, C. Yan and S. Angaiah, *Chin. Chem. Lett.*, 2023, **34**, 108076.
30. H. Wu, X. Wu, R. Wang, X. Chen, R. Lv, L. Fan, F. Kong, L. Ni, G. Diao, R. Xing and M. Chen, *ACS Sustain. Chem. Eng.*, 2024, **12**, 9461-9473.
31. Y. Mao, J. Bai, S. Lin, P. Wang, W. Li, K. Xiao, S. Wang, X. Zhu, B. Zhao and Y. Sun, *Small*, 2024, **20**, 2306615.
32. X. Zhou, Y. Li, J. Chen, Q. Zheng, Y. Huo, F. Xie and D. Lin, *Chem. Eng. J.*, 2023, **471**, 144738.
33. J. Zhang, W. Li, J. Wang, X. Pu, G. Zhang, S. Wang, N. Wang and X. Li, *Angew. Chem. Int. Ed.*, 2023, **62**, e202215654.
34. Y. Zhao, S. Zhang, Y. Zhang, J. Liang, L. Ren, H. J. Fan, W. Liu and X. Sun, *Energy Environ. Sci.*, 2024, **17**, 1279-1290.

35. Y. Chen, C. Lin, X. Chen, Z. Lu, K. Zhang, Y. Liu, J. Wang, G. Han and G. Xu, *Adv. Energy Mater.*, 2024, 2304303.
36. X. Zhao, F. Zhang, H. Li, H. Dong, C. Yan, C. Meng, Y. Sang, H. Liu, Y.-G. Guo and S. Wang, *Energy Environ. Sci.*, 2024, **17**, 3629-3640.
37. Y. Huang, Y. Peng, Q. Ouyang, Q. Feng, H. Wang, D. Zheng, F. Wang, X. Lu and Q. Liu, *Energy Stor. Mater.*, 2024, **70**, 103476.
38. L. Ye, H. Fu, R. Cao and J. Yang, *J. Colloid Interface Sci.*, 2024, **664**, 423-432.
39. Y. Shi, B. Yang, G. Song, Z. Chen, M. Shakouri, W. Zhou, X. Zhang, G. Yuan and H. Pang, *Angew. Chem. Int. Ed.*, 2024, e202411579.
40. C. Chen, T. Wang, X. Zhao, A. Wu, S. Li, N. Zhang, X. Qu, L. Jiao and Y. Liu, *Adv. Funct. Mater.*, 2023, **34**, 2308508.
41. S. Zhao, S. Wang, J. Guo, L. Li, C. Li, Y. Sun, P. Xue, D. Wu, L. Wei, Y. Wang and Q. Zhang, *Adv. Funct. Mater.*, 2023, **33**, 2305700.
42. R. Pan, F. Cui, A. Zheng, G. Zhang, Z. Jiang, Y. Xiong, L. Wei, Q. Zhang, L. Sun and K. Yin, *Adv. Funct. Mater.*, 2023, **33**, 2300619.
43. S. Kong, Y. Li, X. Zhang, Z. Xu, X. Wang, Y. Feng, W. Gong, C. Liu, K. Tian and Q. Li, *Small*, 2023, **19**, 2304462.
44. W. Qiu, Y. Tian, S. Lin, A. Lei, Z. Geng, K. Huang, J. Chen, F. Huang, H. Feng and X. Lu, *J. Energy Chem.*, 2023, **85**, 581-591.
45. T. Wang, S. Li, X. Weng, L. Gao, Y. Yan, N. Zhang, X. Qu, L. Jiao and Y. Liu, *Adv. Energy Mater.*, 2023, **13**, 2204358.
46. C. Liu, W. Xu, C. Mei, M.-C. Li, X. Xu and Q. Wu, *Chem. Eng. J.*, 2021, **405**, 126737.
47. L. Chen, H. Yue, Z. Zhang, Y. Ma, Y. Wang, M. Xu, Y. Huang and G. Yuan, *Chem. Eng. J.*, 2023, **455**, 140679.
48. Y. Mao, B. Zhao, J. Bai, H. Ma, P. Wang, W. Li, K. Xiao, S. Wang, X. Zhu and Y. Sun, *Small*, 2023, **19**, 2207998.
49. X. Zhao, Y. Gao, Q. Cao, F. Bu, J. Pu, Y. Wang and C. Guan, *Adv. Energy Mater.*, 2023, **13**, 2301741.